KANSAS GEOLOGICAL SURVEY
OPEN-FILE REPORT 2001-58

Controls on Ground-Penetrating Radar Reflections in
Pennsylvanian Carbonate Strata:
Implications for Processing and Attribute Analysis

by

Evan K. Franseen
Jianghai Xia
Alan P. Byrnes
Richard Miller
Thomas Weis
Edward Washburn

Disclaimer

Kansas Geological Survey
1930 Constant Avenue
University of Kansas
Lawrence, KS 66047-3726

CONTROLS ON GROUND-PENETRATING RADAR REFLECTIONS IN PENNSYLVANIAN CARBONATE STRATA: IMPLICATIONS FOR PROCESSING AND ATTRIBUTE ANALYSIS

By

Evan K. Franseen, Jianghai Xia, Alan P. Byrnes, Richard Miller, Thomas Weis, and Edward Washburn

Kansas Geological Survey

University of Kansas

1930 Constant Ave.

Lawrence, KS 66047

Kansas Geological Survey Open File Report 2001-58

INTRODUCTION

Outcrops of sedimentary rocks are often studied because they provide detailed data on: 1) processes involved in deposition and diagenesis, 2) geometries and internal bedding character of stratal units, and 3) the nature of facies changes (e.g. grains, fossils, mineralogy). All of these are important to understanding the characteristics that control fluid flow in aquifers and petroleum reservoirs. Outcrop studies typically form the basis for the development of models that are utilized in subsurface studies of analogous sedimentary strata. Although traditional studies of outcrops provide useful information for model development, other methods for outcrop studies are increasingly being sought to extend and refine current models. Ideally, these methods would provide high resolution quantitative data, depict the three-dimensional geometry of stratal units, extend outcrop data into the subsurface, and produce data that are highly correlative with data collected in subsurface studies.

Ground penetrating-radar (GPR) is one method that has great potential as a tool for imaging the near subsurface at a high resolution and in 3-D. GPR is a near-surface, non-intrusive geophysical technique that is similar to seismic reflection but which images the subsurface at a much higher resolution as a result of its use of electromagnetic rather than sound signals. Depending on site characteristics and antennae frequency, GPR can image the subsurface to depths as great as 30 m and can resolve features as small as 0.1 to 1.0 m. These depth and resolution ranges indicate that GPR could be extremely useful for outcrop studies.

Over the last decade ground-penetrating radar (GPR) has been used in environmental, engineering, and groundwater investigations (e.g., Arcone et al., 1998; Olhoeft et al., 1994; Annan, 1996; Young et al., 1997; Powers, 1997; Cardimona et al., 1998; Asprion

and Aigner, 1999; Butler et al., 2000) as well as shallow sedimentary and stratigraphic studies (Arcone, 1996; Smith and Jol, 1992; Pratt and Miall, 1993; Bridge et al., 1995; Sigurdsson and Overgaard, 1996; Liner and Liner, 1997; McMechan et al., 1997; Martinez et al., 1998; Young and Sun, 1999; Vandenberghe et al., 1999; Beres et al., 1999; Augustinus et al., 1999; Dagallier et al., 2000; Kruse et al., 2000; Bano et al., 2000; Van Dam and Schlager, 2000). Although these studies demonstrate the promise and usefulness of GPR for geologic, environmental, and engineering studies, important questions still remain concerning all the factors responsible for the actual appearance and characteristics of GPR reflections and diffractions.

Interpreters of GPR data have traditionally made a basic assumption: most reflection events with continuity (based on amplitude observations) are analogous and directly correlatable to geologic features exposed in immediately adjacent outcrops. It has also been assumed that correlating reflection events interpretable on GPR section to outcrops involves nothing more than visual matching of EM wave reflections (based on amplitude and gross estimations of time-to-depth relationships) to photographs or hand-drawn geologic cross-sections. However, not all coherent GPR reflection events on cross sections (time-offset profiles), that could potentially be interpreted, are within the plane (instrument footprint), are primary reflections, or have the correct geometry that can be directly correlated to features in rock exposures. Our research incorporated several strategies and techniques not previously attempted to groundtruth GPR data and determine controls on GPR reflection events.

A Pennsylvanian reservoir analog in a NE Kansas quarry was selected to conduct experiments within a 3-D grid to test the utility of ground-penetrating radar (GPR) to accurately depict geometry, heterogeneity, and measure petrophysical properties to

provide strategies and methods for the accurate application of GPR to sedimentologic and reservoir analog studies. The initial results and experiments of our study that have implications for GPR applications to the rock record in general are:

1) Wavelet suppression, using the GPR instrument wavelet acquired in air (deterministic deconvolution), successfully eliminates narrow band source wavelet interference and results in clearer depiction of geologic features.
2) Deconvolution of GPR data using measured instrument specific wavelets should be included as a standard GPR data processing step.
3) The instrument wavelet is not dependent on geology or ground coupling. Therefore, once the waveform for a particular GPR instrument is successfully acquired, it can be used as the deconvolution operator in any geologic setting.
4) There is a high degree of direct correlation of GPR reflections with bedding and lithologic changes. Geologic features approaching or exceeding theoretical resolution limits are clearly identifiable on GPR profiles that include deterministic deconvolution in the processing flow.
5) Out-of-plane effects, multiples, and other noise on GPR data are minimal or non-existent in this setting using the deterministic deconvolution in the processing flow.
6) Time-to-depth conversion based on EM wave propagation velocities calculated from moveout curves on CMP data are generally accurate, but can be fine-tuned based on rock property measurements.
7) Petrophysical properties of the rocks in all layers are highly correlated including permeability with porosity and porosity with grain density (reflecting dolomitization).
8) Water-filled porosity exerts significant control on dielectric constant which is important to GPR response.

9) A volumetric-type dielectric mixing (Time-Propagation) model of the strata at the quarry site confirm that this modeling approach is sufficiently accurate for larger scale forward modeling and inversely may allow prediction of rock properties from GPR response using attribute analysis.

SETTING AND METHODS

The study site is located in the Shawnee Rock Company quarry near Bonner Springs, Kansas (Fig 1A). A bench on the upper Farley Member (Pennsylvanian) was selected for the study grid. A 30 m by 30 m two-dimensional grid was designed on a flat bench behind an initial quarry face (BSG1) approximately 2.7 – 3.5 m (9 – 12 feet) thick (Figs. 1B, 1C).

GPR data were initially collected along seven grid lines parallel to the quarry face and seven grid lines perpendicular to the quarry face, each separated by 5 m (Fig. 1B). GPR data were acquired using a MALÅ system using 50 MHz, 100MHz, 200 MHz, and 400 MHz antennas. Data were processed using WinSeis© (a commercial software package developed at the Kansas Geological Survey) complemented with some custom code. Analysis focused on data using the 400 MHz antenna because this frequency provided the highest resolution of targeted geologic features at the study site. A 128-fold vertical stack was acquired every 0.1 m along each line while maintaining a fixed source and receiver separation of 0.6 m with the 400 MHz antenna. A perpendicular-broadside antenna orientation was employed to give the radar section more of a 2-D slice through the subsurface.

Twelve continuous vertical cores, five centimeters in diameter, were taken on 10 x 10-meter spacings within the grid area to provide initial groundtruth for GPR

interpretations (Figs. 1C, 2A). Further groundtruthing of GPR data was accomplished by observing, mapping, and sampling geologic features exposed by successive quarry face exposures (BSG1, BSG2, BSG3, and BSG4) as operators blasted back at 10-m intervals in coordination with our grid and borehole locations (Figs. 2B-E). Cores and outcrops were sampled for lithologic, diagenetic, porosity, hydraulic permeability, minipermeameter, water saturation, and dielectric constant data.

A total of 78 horizontal holes were drilled in key locations on three exposed quarry faces where GPR data were acquired before and after conductive steel rods, 1.5 m in length, were placed in the holes. Diagnostic GPR responses from the horizontal steel rods served as known reflectors and provided ultimate groundtruthing of GPR data. The steel bars provided critical information for: 1) confirmation and nature of specific geologic reflection events in the GPR data, 2) GPR resolution limits, 3) accuracy of velocities calculated from CMP data, and 4) determining if any multiples occurred in the GPR data.

General Stratal and Facies Characteristics

Upper Farley strata are vertically exposed for approximately 3 meters on the quarry face and characterized by medium (< 0.15 m) to thickly (0.3 – 0.9 m) bedded carbonates separated by thin (< 2.5 cm) shale partings and stylocumulates (Figs. 3, 4). A characteristic of upper Farley strata is the extensive lateral continuity of the generally horizontal to wavy horizontal bedding. Shale partings and stylocumulates at bedding planes are generally consistent, but locally come and go laterally. The nature of the strata made it ideal for the purposes of our study. Details of stratal and lithologic characteristics are discussed in later sections.

DETERMINISTIC DECONVOLUTION

"Ringing" (due to narrow bandwidth and source waveform) in a GPR section dramatically limits resolution, and increases the potential for misinterpretations, thereby constraining the usage of GPR. Deconvolution can be used to compress the basic source wavelet resulting in improved temporal resolution. Although there are many different deconvolution methods with application histories in seismic reflection data processing, deconvolution is rarely used successfully in GPR studies of real-world sites due to source wavelet assumptions inherent to most deconvolution models. Our study developed the following convolution model using a GPR instrument wavelet acquired in air. The following section briefly describes some of the key steps utilized in our study for successful application of deterministic deconvolution. For further details on deterministic deconvolution used in our study, see Xia et al. (2001a; 2001b).

Convolution Model

Assuming no noise, GPR data are the convolution of the instrument or source wavelet with the earth's reflectivity series:

$x(t) = w(t)*e(t)$ (1)

where

$x(t)$ = recorded GPR data

$w(t)$ = instrument wavelet

$e(t)$ = earth's reflectivity series

$*$ = denotes convolution.

In the frequency domain, Eq. 1 can be written as:

$X(f) = W(f)E(f)$ (2)

where

X(f) = the Fourier transform of x(t)

W(f) = the Fourier transform of w(t)

E(f) = the Fourier transform of e(t).

If w(t) is known and its spectrum W(f) has no zeros within a specific range, an earth reflectivity series can be determined using a deterministic deconvolution:

$$E(f) = X(f)/W(f) \qquad (3)$$

and the inverse Fourier transform

$$e(t) = F\text{-}1[E(f)] \qquad (4)$$

where

F-1 = the inverse Fourier transform.

Acquisition of the Source Wavelet

An MALÅ system with a 370-V transmitter, 400 MHz antennas, and 3348 MHz sampling frequency was used in our study. Instrument wavelets were acquired in an open area void of environmental and/or culture noise. Acquisition of a clean instrument wavelet is critical to the effectiveness of deterministic deconvolution. A 512-fold vertical stack was used to minimize the contribution of random noise during the acquisition of a representative wavelet. Initially, to capture the source wavelet, a signal search was performed with the transmitter antenna and receiver antenna separated by 0.3 m, 0.6 m, and 0.9 m respectively using conventional facedown on the ground coupling (Fig 5A). Next, to acquire the actual source wavelets, the antennas were placed face to face to acquire wavelets in the air at 0.3, 0.6, 0.9 m respectively (Fig 5B). Trial applications determined that the wavelet extracted with 0.3-m separation produced the best results for 400 MHz antennas. Successful acquisition of the basic source wavelet unique to this radar equipment is indicated by the well-behaved spectrum of the 400 MHz antenna

wavelet (no zero or near zero values in the designed frequency range spectrum), and a dominant frequency of 300 MHz (Fig. 6). This can then be used for direct and stable application of deterministic deconvolution (Eq. 3 of the Convolution Model) to suppress the source wavelet in GRP data. It is important to note that the instrument wavelet is not dependent on geology or antenna ground coupling. Therefore, a waveform acquired in air can be used as the deconvolution operator in any geologic setting.

Verification of Deterministic Deconvolution from the Study Site

A variety of experiments were conducted using steel rods, 1.5 m in length and 4.4 cm in diameter, inserted into holes drilled horizontally into the quarry face. A specially designed air-drilling unit was used to drill holes that allowed rods to be driven snuggly into place (Fig. 7A). GPR data were acquired before and after the conductive steel rods were placed in holes (Fig. 7B). Reflections/diffractions from the rods on the GPR data provided absolute bearings as to the exact location in the 3-D subsurface being imaged. Comparison to measured locations of rods on the quarry face determined whether coherent GPR events were due to geologic features or were noise. The steel rods were variously arranged vertically or laterally along horizons in the quarry face exposures to determine the nature of GPR response and for use in accurately calibrating GPR data to known locations as measured on the quarry face (Figs. 8, 9, 10). The steel rods proved extremely useful for verification that including a deterministic deconvolution processing step improved the quality of GPR images over images that are conventionally processed using only scaling and bandpass filtering.

One example using steel rods demonstrates the improved resolution of GPR data using deterministic deconvolution. This experiment consisted of six vertically aligned steel rods in quarry face BSG3 (Fig. 8A). We acquired GPR data along a 6-m trace, 1 m

behind the quarry face containing the steel rods. The conductive rods cause reflections that appear as hyperbolas on GPR profiles. Although the apex of the hyperbolas should be indicative of the precise location of the rods, the locations (horizontal and vertical) of the apex of the hyperbola on the non-deconvolved GPR profile are skewed compared to the true rod locations (Figure 8B). The average velocity of EM wave propagation in the limestone at this site is 0.1 m/ns, which for the 400 MHz antenna equates to a maximum potential vertical resolution of around 0.25 – 0.30 m. Theoretically, two reflectors closer than 0.25 – 0.30 m will not be resolvable because any reflected events with time duration equal to or longer than 1/2 the width of the main peak will interfere with each other, smearing, splitting, and/or misplacing reflections in time and/or space. With this limitation in resolution, the six rods on the non-deconvolved GPR data can only be located within confidence of ± 10 cm vertically and ± 20 cm horizontally (Fig. 8B).

In contrast, after including deterministic deconvolution in the processing flow (Fig. 8B), the peaks of the four shallowest hyperbolas distinctly and correctly represent the locations of the corresponding four rods both horizontally and vertically. Using a normal moveout velocity calculated from a nearby CMP gather (0.097m/ns), the true depths of the first four rods can be located within a few centimeters on the GPR profile. It is also possible to locate the two deepest rods even though they are considered relatively deep (considering their size and penetration limitations for antennas of this frequency) and are less than one-quarter wavelength apart.

The improvement in resolution after deterministic deconvolution is further demonstrated by comparison of deconvolved and non-deconvolved GPR traces of an entire quarry face within our grid (Fig. 11A, B, C). GPR data were again acquired along a line one-meter behind the quarry face. CMP data with 60-trace gathers and maximum

source and receiver antenna separation of 6 m were acquired at eleven intersection points of the GPR survey grid. Time to depth conversions are based on EM wave propagation velocities calculated from moveout curves on the CMP data. Accuracy of these conversions was confirmed by comparing surveyed horizontal rod locations along the BSG1 face with locations calculated from the GPR measured velocity.

Some reflections on non-deconvolved GPR data (Fig. 11C) appear to correlate with the stratigraphy shown on the photomosaic, however much of the GPR data are very difficult to interpret correctly due to the dominance of a very complex arrival pattern characteristic of wavelet interference, and possible out-of-the-plane energy. Based on the results of the steel rod experiment discussed above, many of these complexities are a byproduct of the data resolution and associated wavelet interference, which makes it difficult to interpret most of the bedding on this section. Results from the rod experiments also indicate that interpretations are further complicated by the inaccurate vertical and horizontal locations of geologic features imaged by non-deconvolved GPR data.

Resolution of reflection response, positions of bed boundaries, and rod locations is considerably improved after deterministic deconvolution (Figure 8C). Data using the known locations of the steel rods indicate that: 1) reflection events in these GPR data are from specific geologic features (multiples are absent); 2) the locations of beds along the BSG1 face are spatially accurate along the entire deconvolved GPR trace as confirmed by measurements from the quarry face.

GPR RESULTS AND RELATION TO LITHOLOGY

This section describes lithology, geologic features, and results of GPR profiles from two of the quarry faces that were exposed within the grid. We focus on the results of GPR profiles using the 400 MHz antennas because they provide the highest resolution of features exposed on the quarry faces. Theoretically, using the 400 MHz antenna, resolution should be smaller than ~15 cm, and potentially greater, depending on dielectric constant (Fig. 12).

Lithologic Features

In general, the upper Farley strata at the study site are characterized by carbonate beds that are separated by thin shale seams. However, some horizons show more complex and vertical and lateral variability. The twelve cores taken within the grid were described in detail for further facies characteristics that may be important for GPR response (Fig. 13). Facies were divided into the following categories: 1) Shale/Clay, 2) Calcareous Shale/Clay, 3) Shaly Limestone, 4) Mudstone (carbonate), 5) Mudstone/Wackestone, 6) Wackestone, 7) Wackestone/Packstone, 8) Packstone, 9) Packstone/Grainstone, and 10) Grainstone. Using a digital lithofacies classification system (Fig. 13), the cores were described at 0.1 foot intervals. These digital descriptions were used to visually represent the rocks, to model petrophysical properties for dielectric modeling, and to compare rock properties with GPR profiles from quarry faces.

Comparison of Quarry Face and GPR Results

Each quarry face was mapped in detail to document bedding characteristics and traceability across the exposed face (Figs 14, 15). Eleven major traceable bedding planes were identified on each of the four exposed quarry faces. These beds are labeled from top to bottom: A, *(star), B, • (dot), C, E, D, F, G, H, and X. Solid lines represent

distinct, traceable bedding planes (most characterized by distinct bedding plane breaks with distinct shale partings), dashed lines reflect bedding planes that are less distinct and shale partings are typically thinner or more diffuse, and dotted lines represent inferred bedding planes, where no distinct lithologic break is evident. Orange dots show the locations of the horizontal steel bar experiments. Core descriptions are included to provide facies data. The bedding features as mapped on the quarry faces are shown directly overlain on the 400 MHz GPR profiles from the same faces; exact locations are confirmed by steel bar experiments. Some adjustment in overlaying the data on the GPR sections had to be made, and 100 percent match was not possible due to: 1) The quarry face exposures contain some three dimensionality (not a straight plane) that gives some curvature to bedding features on the mosaics, whereas the GPR data were collected along a straight line, 2) the GPR data were taken approximately 1-m behind the quarry face exposure so that there may be some change in bedding character in that direction behind the exposure, 3) core locations are matched to the quarry face exposures as close as possible but may not reflect exact location due to the nature of the quarry face after blasting. Overall, the comparison with quarry facies data indicates a high degree of direct correlation of GPR reflections with bedding and lithologic changes. The following section discusses and compares bedding features as documented on the quarry faces and their representation on the GPR data.

On the quarry face, the * (star) and ● (dot) bedding planes are very distinct and sharp, and laterally traceable across the entire face. Both bedding planes contain distinct shale layers and clay laminations along the entire trace of the beds. Diffuse clay and clay intermixed in carbonate is common in strata immediately adjacent to these bedding planes. Consistent with reflectivity estimations, the * (star) and ● (dot) horizons should

be, and are, strong, laterally continuous reflections on the GPR profiles from the two quarry face examples (Figs. 14, 15).

Beds A and B are mostly distinct, laterally traceable bedding planes on quarry exposures. However, there is some lateral variation along these bedding planes. Locally, the bedding planes contain distinct shale layers and clay laminations. Elsewhere, the bedding planes may contain little clay (only marked by diffuse clay or some minor clay laminations). Based on this lateral variation in shale concentration, these bedding planes would be expected to possess some variability in reflection wavelet character as a function of the differing shale concentrations. On the GPR profile, bedding planes A and B are confidently identified and, as expected, their reflection character varies laterally (Figs. 14, 15).

Below the • (dot) bedding plane, bedding character is more complex due to highly variable shale content along bedding planes, additional bedding planes (unlabeled) that appear between the major labeled bedding planes, and bedding planes that converge, or die out. Several bedding planes (D, F, X) are relatively distinct, sharp breaks and generally traceable across most of the quarry face exposures. However, there is some lateral variation along these bedding planes. Locally, the bedding planes contain distinct shale layers and clay laminations. Elsewhere, the bedding planes may contain little clay (only marked by diffuse clay or some minor clay laminations). As expected, the reflection character varies laterally for bedding planes D, F and X on the GPR profiles. Further complexities occur due to added minor clay seams that occur near these beds, and convergence of major bedding planes beyond the resolution of the deconvolved 400 MHz GPR data (< 10 cm; 0.3 in), which likely adds complexity in reflection character due to signal interference.

Bedding planes C, E and G, H show the most complexity on quarry face exposures. These bedding planes locally die out laterally, other bedding planes locally occur between these horizons, there is highly variable shale content along the bedding planes, and there is geometric complexity (pinching, swelling, bedding plane convergence, additional minor bedding planes). Accordingly, GPR reflection characteristics and geometry for these horizons is expected to be very complex. GPR data on Figures 14 and 15 both show the most complexity in reflection character at these horizons. The additional minor clay seams (unlabeled) that occur near these beds, and convergence of major bedding planes beyond the resolution of the deconvolved 400 MHz GPR data (< 10 cm; 0.3 in), likely add complexity to reflection character due to signal interference. Although exact tracing of beds is difficult, confident identification of the general location of these complex horizons and the similarity in complexity on outcrop and complexity on GPR indicates that the GPR reflections are responding to the geological features.

ROCK PROPERTIES, GPR RESPONSE, & FORWARD MODELING OF GPR RESPONSE

Dielectric constant is a critical GPR parameter because it controls the electromagnetic wave propagation velocity through a material, the reflection coefficients at interfaces, and affects the vertical and horizontal imaging resolution. Knowledge of dielectric constant values of materials aids in understanding and interpreting GPR images.

Dielectric constants in rocks are primarily a function of mineralogy, porosity, pore fluids, frequency, geometries and electrochemical interactions between the components. The close match of strong GPR reflections to clay-rich lithology as discussed in the above section suggests clay content and mineralogy is a strong control. However, the

clay minerals present in the Farley are mainly illite/mica, kaolinite, and some smectite, (Mckirahan et al., 2000). The dielectric constant for illite/mica is 6.4 (Martinez and Byrnes, 2001) and kaolinite is 11.8 (Olhoeft, 1989), whereas the dielectric constant for calcite and dolomite ranges from 6.4 to 8.5 (Martinez and Byrnes, 2001; Olhoeft, 1989). Therefore, the similarity in dielectric constants between the clays that are present at the study site and the carbonate rocks indicates that mineralogy alone cannot account for the strong reflections that occur.

Martinez and Byrnes (2001) have recently shown the significant influence of water saturation and porosity and the lesser influence of mineralogy on bulk dielectric constant (Fig. 16) and, therefore, are primary controls on GPR response, including two way travel time, reflection coefficient amplitude across interfaces of different materials, and vertical and horizontal imaging resolution.

Petrographic studies and a suite of petrophysical properties were measured on samples from cores to further understand the lithologic and petrophysical controls on GPR response. Core plug petrophysical analyses indicate there is a good correlation between porosity and permeability for all beds (Fig. 17). Furthermore, increasing porosity (ϕ) and permeability (k) are associated with dolomitization (Fig. 18). Increasing dolomitization is associated with increasing ϕ for $\phi > 10\%$. Increasing dolomite content is also associated with higher k at any given ϕ for $\phi > 10\%$. Variance in density for any given ϕ is not strongly influenced by argillaceousness. However, horizontal partings along shale beds also create high porosity and permeability. Core plug and miniprobe permeability measurements also indicate that the middle of the studied quarry exposures generally have higher porosity and permeability values as compared to the upper and lower (to 11 foot depth) portions of the studied interval (Fig. 19). Figures 20 and 21

illustrate lithologies, porosity, and grain density (dolomite) relationships and associated GPR response. There is a general consistency in rock properties and GPR response between all cores taken within the grid (Figs. 20, 22). A strong GPR response is generally associated with the higher porosity dolomite intervals and shale-rich bedding planes. Clean carbonates with less dolomite are less porous and GPR response tends to be weaker.

Although there appears to be a clear relationship between higher porosity and strong GPR response water saturation in the pore space exerts significant control on dielectric constant. Water saturations, measured from samples collected on fresh quarry outcrop faces, approached 100% in shaly intervals and in the higher porosity carbonates (higher % dolomite) for several inches adjacent to these shale aquitards (Fig. 23). Water saturations in clean carbonates were much lower (generally 40% or less). The strong GPR reflections at shale bed contacts are interpreted to result from the higher porosity associated with dolomitization and clay bedding planes/partings and high water saturation states associated with those horizons.

The high degree of direct correlation of GPR reflections with geologic features and rock properties provides the opportunity to do forward modeling to determine which rock properties exert dominant control on reflectivity. Results from forward modeling, compared to and calibrated with actual GPR response from the grid, can in turn be used for inversely modeling expected reflection coefficients, two-way travel-times, and vertical and spatial imaging. The inverse modeling results can be used to predict lithology and rock properties based on GPR attributes away from control points.

Dielectric constant mixing models allow prediction of bulk dielectric properties of complex earth materials based on the dielectric properties of constituent materials. A dielectric mixing model that is highly useful and easy to construct for geologic materials is the Time-Propagation (TP) model, a volumetric-type dielectric mixing model. The input parameters for TP modeling are easily obtained, the mathematical equation to calculate bulk dielectric-constant values is simple, and the results of the TP model are very similar to observed values (Martinez and Byrnes, 2001).

The mathematical equation describing the TP dielectric mixing model is:

$E_r = [\Sigma\ V_i(E_{ri})^{0.5}]^2$

where E_r is the dielectric constant and V_i and E_{ri} are the bulk volume fraction and dielectric constant of the ith component (Knoll, 1996). The TP model is a specific case of the more general Lichtenecker-Rother (1931) equation:

$E_r = [\Sigma\ V_i(E_{ri})^{\alpha}]^{1/\alpha}$

where a geometric factor that relates the direction of the effective layering of components to the direction of the applied electrical field, is 0.5. The TP model does not account for variations in frequency and is valid only for low conductivity ($\sigma < 10$ mS/m), non-magnetic (i.e., $u_r=1$) materials. Due to the high E_r of water ($E_r = 81$), water saturation and porosity play a critical role in bulk E_r. Figure 24 shows the results of TP modeling for this study and the close match of measured and observed petrophysical values.

Electromagnetic impedance equals the square root of dielectric constant. Using EM impedance, the reflection coefficient (RC) of GPR signals in nonmagnetic material can be calculated using the relationship:

$RC = [(E_{r1})^{1/2} - (E_{r2})^{1/2}]/ [(E_{r1})^{1/2} + (E_{r2})^{1/2}]$

where E_r is the dielectric constant of the upper media, and E_{r2} is the dielectric constant of the lower media. This equation describes the strength of single-fold reflections at interfaces of materials of different lithology or water saturations (i.e., different bulk dielectric constants).

Results of initial TP modeling for reflection coefficients are shown in Figure 25. These results indicate that water-saturation states are the primary control on GPR response because of the high dielectric constant of water. If the site were completely dry, the model results indicate that porosity and mineralogy alone would not produce the response seen on the GPR data. Many reflections that are strong on the observed GPR profiles are subdued in the model, and there is a weak signal-to-background noise ratio in the model. Modeling using a full-water saturated condition also does not provide a match between modeled and predicted GPR response. If the rocks were water-saturated a contact between a high porosity and underlying low porosity rock, similar to a carbonate-shale contact, would produce a peak to trough response. This is the opposite reflection of that observed on GPR profiles. In addition, in fully water-saturated carbonates, all contacts between high and low porosity carbonate would produce strong reflections, which was not observed in the field.

In the final model, bulk E_r was calculated for a vertical profile using measured porosity and argillaceousness values, and water saturation values of 100% for shale bedding planes and 40% water saturation for the carbonate strata as measured at the 10m-10m location. Modeled high reflection coefficients at shale/carbonate bedding plane contacts (resulting in a strong GPR response) match closely with the observed GPR signal and amplitude. This supports the interpretation that water at shale partings and

bedding planes, and high porosity in dolomite that occurs adjacent to shale horizons combine to be the primary controls on strong GPR reflections.

These results provide confidence for further interpreting details on the collected GPR data that were not obvious in the field. Discontinuous and subtle reflectors between the main traceable layers are likely areas of water saturated shale partings and/or porous dolomite intervals (at least partially saturated) that affect heterogeneity within the setting. The understanding of controls on GPR reflection provides the opportunity to use GPR attributes for further interpretation of lithologic, porosity, and resultant water saturation state and heterogeneity of this reservoir analog at high resolution between control (outcrop and core) points.

CONCLUSIONS

1) Exposures of a Pennsylvanian reservoir analog, characterized by horizontally bedded carbonates separated by thin shale partings and stylocumulates, provided an opportunity to conduct studies and experiments to analyze the effectiveness of GPR for accurately depicting stratal characteristics, heterogeneity, and petrophysical properties.

2) A convolution model was developed using a unique GPR instrument wavelet acquired in air. Wavelets for 400 MHz antenna (0.3 m spacing) and 200 MHz antenna (0.9 m spacing) possessed well-behaved spectral properties. A wavelet suppression procedure (deterministic deconvolution) was then implemented during processing of GPR data.

3) Once a wavelet is acquired and defined for a particular antenna, it can be permanently stored and used for any geologic setting. Changes in geologic material being imaged or ground coupling will have no impact on the source wavelet.

4) Deterministic deconvolution, using the acquired instrument wavelet, successfully suppressed narrow-band source-wavelet interference and resulted in clearer depiction of geologic features. Detailed comparison of quarry exposures of successive faces and conductive steel bar experiments confirmed that GPR data processed using deterministic deconvolution provided superior GPR profiles compared to conventionally processed GPR data (only scaled and AGC bandpass filtered).

5) Out-of-plane effects, multiples, and other noise on GPR data are minimal or non-existent in this setting based on: A) comparison of two GPR data sets acquired along the same line before and after the blasting of successive quarry faces, and B) data from conductive steel bar experiments.

6) There is a high degree of correlation of GPR reflections with bedding and lithologic changes. Theoretically, resolution should be finer than ~15 cm, depending on dielectric constant, using the 400 MHz antenna. Major geological features identified on quarry walls (~ 3-3.5 m vertical exposures), even those as closely spaced as ~10 cm (0.3 in.), are resolvable on the GPR data and can be confidently correlated.

7) Time-to-depth conversion based on EM wave propagation velocities calculated from moveout curves on CMP data are generally accurate as confirmed by steel bar experiments. However, petrophysical measurements indicate that the middle of the studied quarry exposure has generally higher porosity and permeability values as compared to the upper and lower portions of the studied interval. These data can be used for refining velocity calculations.

8) Petrophysical properties of the rocks in all layers are highly correlated including permeability versus porosity and porosity versus grain density. Increased porosity is generally associated with dolomite; much of the dolomite is associated with clay-rich intervals. Higher porosity also occurs at partings in and bounding clay-rich beds.

9) Rock properties and GPR response for data collected from all faces is consistent. Strong GPR response is generally associated with higher porosity dolomitic and clay-rich intervals that typically occur at or near bedding planes. Clean carbonates with less dolomite are less porous and exhibit few contrasts in dielectric constant and thus few strong reflections.

10) Bulk dielectric constant is primarily controlled by water saturation, porosity and mineralogy. Water saturations, measured from samples collected on fresh outcrop face, approached 100% in shaly intervals and in the carbonate for several inches adjacent these shale aquitards. The high dielectric constants associated with these high water saturations and clays significantly control the reflectivity.

11) A volumetric-type dielectric-mixing model (Time-Propagation) allows prediction of bulk dielectric properties based on the dielectric properties of constituent materials. Results using this forward modeling approach show that a dry or fully water-saturated outcrop does not exhibit the observed GPR response. A modeled response for a profile with ~40% saturation in the limestone and 100% in the shales exhibits strong reflectance coefficient values at the shale beds and closely matches observed GPR response indicating water saturation and porosity are primary controls on GPR response.

12) Once confidence has been gained that GPR data are of sufficient quality and accurately represent geologic features and rock properties, the forward modeling results can be used for inversely modeling expected reflection coefficients, two-way travel-times, and vertical and spatial imaging resolutions for field GPR and reservoir analog studies. Efforts along these lines are being used in conjunction with the abundant GPR data collected in the field for depicting stratal relationships and heterogeneity in 3-D, and at very high resolution, for this reservoir analog study site.

ACKNOWLEDGEMENTS

We thank Shawnee Rock, Inc., Bonner Springs, Kansas, especially Frank Rockers, and Owen Crome, for kindly providing access to the quarry study site, cooperating in design of the project, and assistance during data acquisition. This study was funded by the National Science Foundation (EAR 9912062).

REFERENCES

Annan, A.P., 1996, Ground penetrating radar (workshop notes): Sensors & Software Inc., Canada.

Arcone, S.A., 1996, High resolution of glacial ice stratigraphy: A ground-penetrating radar study of Pegasus Runway, McMurdo Station, Antarctica: Geophysics, 61, 1653-1663.

Arcone, S.A., Lawson, D.E., Delaney, A.J., Strasser, J.C. and Strasser, J.D., 1998, Ground-penetrating radar reflection profiling of groundwater and bedrock in an area of discontinuous permafrost: Geophysics, 63, 1573-1584.

Asprion, U., and Aigner, T., 1999, Towards realistic aquifer models: three-dimensional georadar surveys of Quaternary gravel deltas (Singen Basin, SW Germany): Sedimentary Geology, 129, 81-297.

Augustinus, P.C., and Nichol, S., 1999, Ground-penetrating radar imaging of Pleistocene sediments, Boco Plain, western Tasmania: Australian Journal of Earth Sciences, 46, 275-282.

Bano, M., Marquis, G., Nivier, B., Maurin, J.C., Cushing, M., 2000, Investigating alluvial and tectonic features with ground-penetrating radar and analyzing diffractions patterns: Journal of Applied Geophysics, 43, 33-41.

Beres, M., Huggenberger, P., Green, A.G., and Horstmeyer, H., 1999, Using two- and three-dimensional georadar methods to characterize glaciofluvial architecture: Sedimentary Geology, 129, 1-24.

Bridge, J.S., Alexander, J., Collier, R. E. LL., Gawthorpe, R.L., and Jarvis, J., 1995, Ground-penetrating radar and coring used to study the large-scale structure of point-bar deposits in three dimensions: Sedimentology, 42, 839-852.

Butler, J., Franseen, E., Xia, J., Schulmeister, M., Zheng, L., Weis, T., Byrnes, A., Healey, J., and Miller, R., 2000, Experimental assessments of the utility of direct-push profiling and ground-penetrating radar for hydrostratigraphic investigations: SEPM/IAS research Conference Environmental Sedimentology Hydrogeology of Sedimentary Aquifers, Santa Fe, NM, September 24-27, 26-27.

Cardimona, S.J., Clement, W.P., and Kadinsky-Cade, K., 1998, Seismic reflection and ground-penetrating radar imaging of a shallow aquifer: Geophysics, 63, 1310-1317.

Dagallier, G., Laitinen, A.I., Malartre, F., Campenhout, I.P.A.M., and Veeken, P.C.H., 2000, Ground penetrating radar application in a shallow marine Oxfordian limestone sequence located on the eastern flank of the Paris Basin, NE France: Sedimentary Geology, 130, 149-165.

Knoll, M. D., 1996, A petrophysical basis for Ground-penetrating radar and very early time electromagnetics, electrical properties of sand-clay mixtures: unpublished Ph.D. dissertation, University of British Columbia, 316p.

Kruse, S.E., Schneider, J.C., Campagna, D.J., Inman, J.A., and Hickey, T.D., 2000, Ground penetrating radar imaging of cap rock, caliche and carbonate strata: Journal of Applied Geophysics, 43, 239-249.

Lichtenecker, K., and Rother, K., 1931, Die Herleitung des logarithmischen Mischungsgesetz es aus allgemeinen Prinzipien der stationären Strömung: Physikalische Zeitschrift, v. 32, p. 255-260.

Liner, C.L., and Liner, J.L., 1997, Application of GPR to a site investigation involving shallow faults: Leading Edge, 16, 1649-1651.

Martinez, A., and Byrnes, A. P., 2001, Modeling Dielectric-constant Values of Geologic Materials--An Aid to Ground-penetrating Radar Data Collection and Interpretation: Current Research in Earth Sciences, Kansas Geological Survey Bulletin 247, part 1. http://www.kgs.ukans.edu/Current/2001/martinez/martinez1.html.

Martinez, A., Franseen, E.K., and Beaty, D.S., 1998, Application of Ground-Penetrating Radar to Sedimentologic and Stratigraphic Studies: Examples from Pennsylvanian Siliciclastics and Limestones in Kansas: Proceedings Vol. 2, Seventh International Conference on Ground Penetrating Radar, University of Kansas, Lawrence, Kansas, p. 687-692.

McKirahan, J., Goldstein, R.H., and Franseen, E.K., 2000, Sequence Stratigraphy of the Lane-Island Creek Shales and the Farley Limestone in Northeastern Kansas and Geologic Factors Affecting the Quality of Limestone Aggregates: K-TRAN Report No. KU-97-1, 236 p.

McMechan, G.A., Gaynor, G.C., and Szerbiak, R.B., 1997, Use of ground-penetrating radar for 3-D sedimentological characterization of clastic reservoir analogs: Geophysics, 62, 786-796.

Olhoeft, G.R., Powers, M.H., and Capron, D.E., 1994, Buried object detection with ground penetrating radar: Proc. of Unexploded Ordnance (UXO) detection and Range Remediation Conference, Golden CO, May 17-19, 1994, 207-233.

Olhoeft, G. R., 1989, Electrical properties of rocks: in, Physical Properties of Rocks and Minerals, Y. S. Touloukian, W. R. Judd, and R. F. Roy, eds., New York, New York, Hemisphere Publishing Corporation, p.257-329.

Powers, M. H., 1997, Modeling frequency-dependent GPR: The Leading Edge, 16, 1657-1662.

Pratt, B.R., and Miall, A.D., 1993, Anatomy of a bioclastic grainstone megashoal (Middle Silurian, southern Ontario) revealed by ground-penetrating radar: Geology, 21, 223-226.

Sigurdsson, T., and Overgaard, T., 1996, Application of GPR for 3-D visualization of geological and structural variation in a limestone formation: Proceedings, Sixth International Conference on Ground Penetrating Radar, Sendai, Japan, 39-42.

Smith, D.G., and Jol, H.M., 1992, Ground-penetrating radar investigation of a Lake Bonneville delta, Provo level, Brigham City, Utah: Geology, 20, 1083-1086.

Van Dam, R.L., and Schlager, W., 2000, Identifying causes of ground-penetrating radar reflections using time-domain reflectometry and sedimentological analyses: Sedimentology, 47, 435-450.

Vandenberghe, J., and van Overmeeren, R.A., 1999, Ground penetrating radar images of selected fluvial deposits in the Netherlands: Sedimentary Geology, 128, 245-270.

Xia, J., Weis, T., Franseen, E.K., and Miller, R.D., 2001a, Ground truth of ground-penetrating radar data at a limestone quarry: Symposium on the Application of Geophysics to Engineering and Environmental Problems (SAGEEP 2001), Denver, Co, March 4-7, 2001, 12 pp. Proceedings published on CD.

Xia, J., Franseen, E.K., Miller, R., and Weis, T., 2001b, Improving Ground-Penetrating Radar Data for Stratigraphic Studies Using Deterministic Deconvolution: An Example from Pennsylvanian Carbonate Strata in Kansas: Kansas Geological Survey Open-file Report 2001-35, 27 p.

Young, R. A., Deng, Z., Marfurt, K. J. and Nissen, S. E., 1997, 3-D dip filtering and coherence applied to GPR data: A study: The Leading Edge, 16, 921-928.

Young, R. A., and Sun, J., 1999, Revealing stratigraphy in ground-penetrating radar data using domain filtering: Geophysics, 64, 435-442.

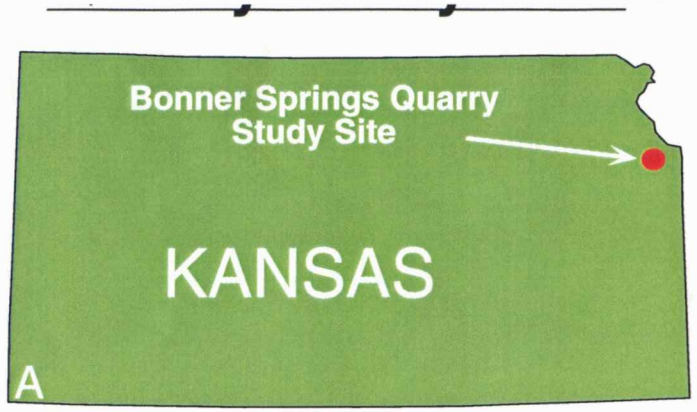

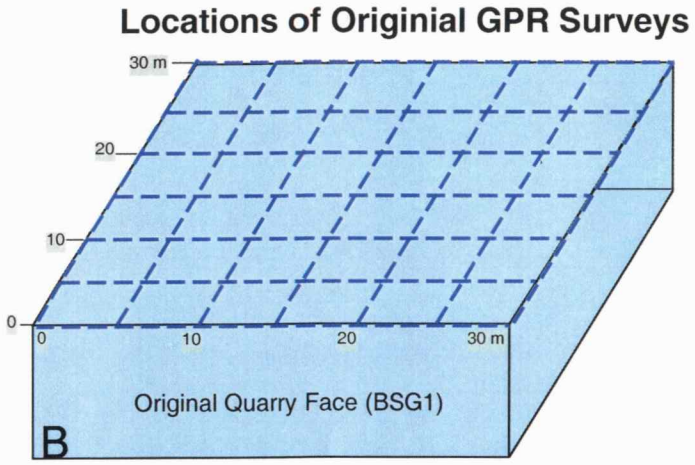

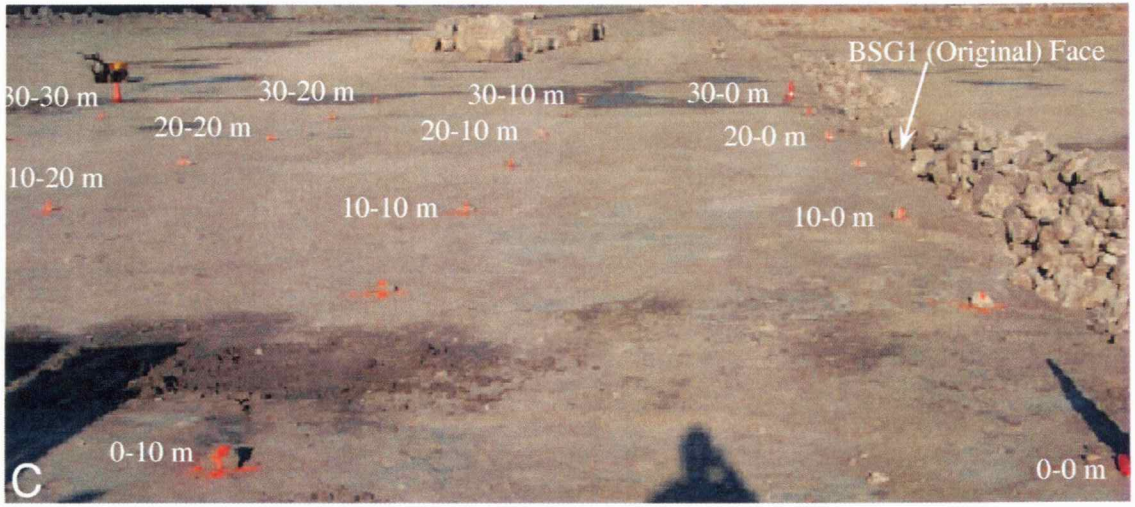

Figure 1: A) Study site location. B) and C) A 30 x 30 m grid was set up on a flat bench just behind the original quarry face. The surface was cleaned as much as possible of any debris and shale material. Initially, seven GPR lines were collected parallel to the quarry face and seven lines perpendicular to the quarry face, each separated by 5 m. Antennas of 50,100, 200, and 400 Mhz were used for each line. Additional GPR data were collected in conjunction with steel rod bar experiments and as successive faces of quarries were exposed.

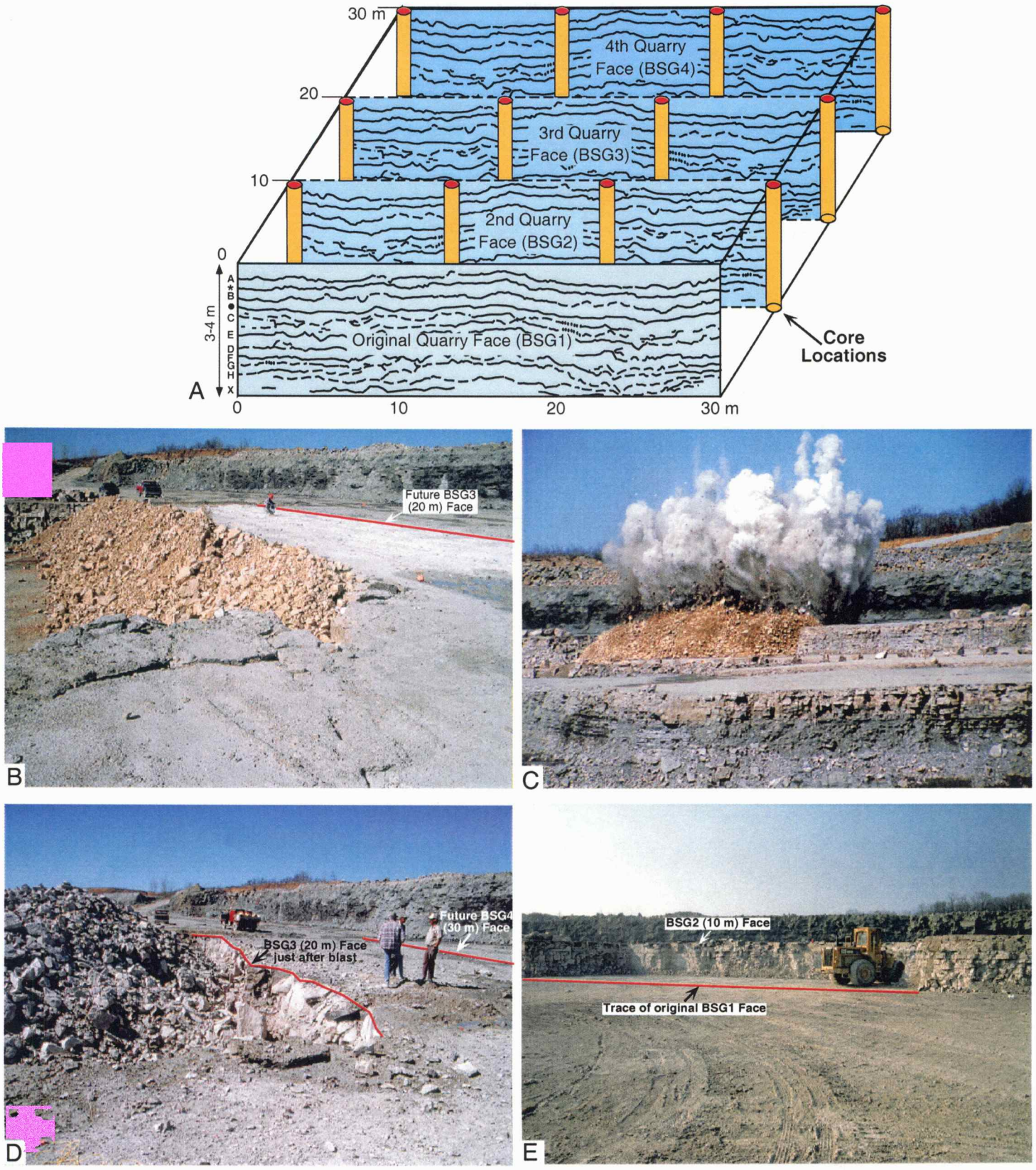

Figure 2: A) Locations of successive quarry faces and cores. 12 cores were obtained within the grid at 10 meter intervals behind the original quarry face. Those locations coincided with future quarry faces to be exposed through repeated blasting by quarry operators within our grid design. B) Planting of explosives within the grid in preparation of blasting back to the BSG3 (20 m) face. Rocks are piled up in front of the BSG2 (10 m) face to help control the direction of blast. C) Blasting to expose the BSG3 (20 m) face. D) Just after the blasting to expose the BSG3 (20 m) face. Quarry equipment then clears blast debris to expose the face for stratigraphic,sedimentologic and additional GPR work associated with the newly exposed face. E) Clean exposure of the BSG2 (10 m) face after blasting and cleanup by quarry operators.

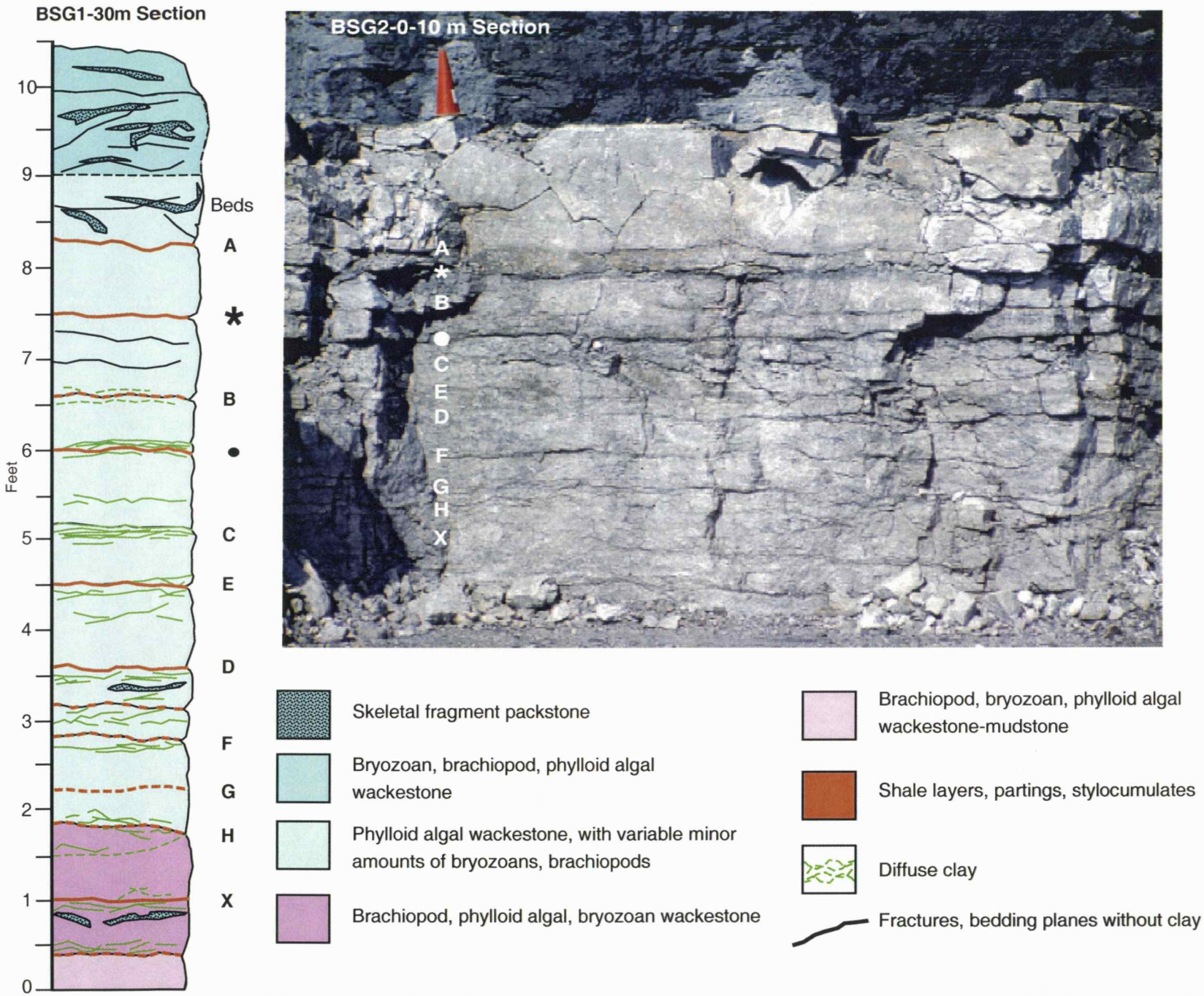

Figure 3: Example stratigraphic section and photograph of the initial quarry face showing lithologic and stratigraphic nature of the upper Farley unit.

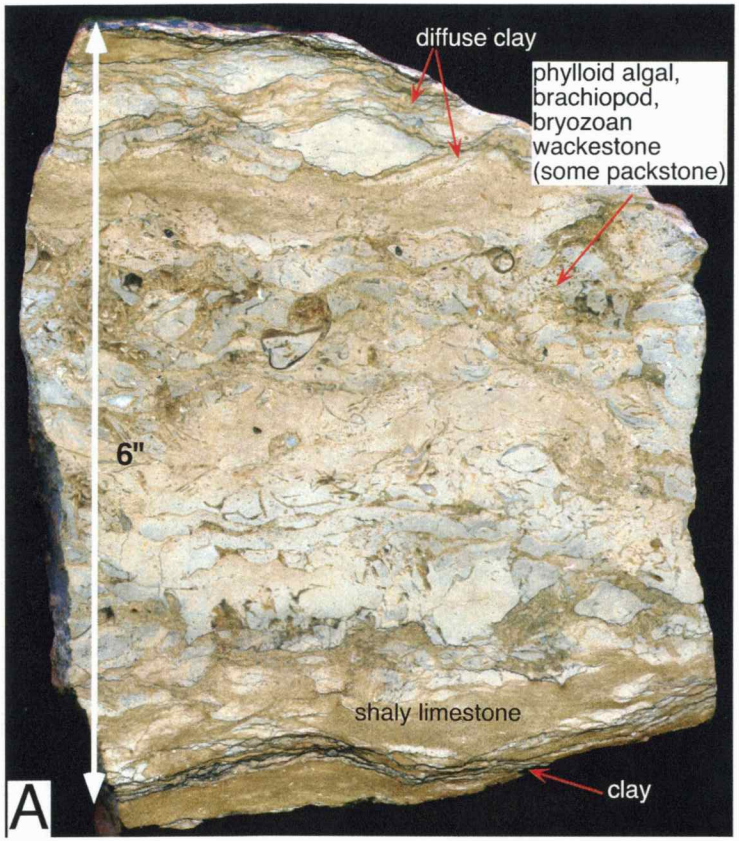

Figure 4: Limestone beds are typically composed of skeletal wackestone and packstone consisting predominantly of phylloid algae, bryozoans, brachiopods (A). Shale beds, partings and stylocumulates are commonly diffuse into adjacent limestone over the scale of < 2.5 cm to ~7.5 cm (A, B, C). Shale-rich bedding planes and diffuse clay areas were saturated with water after rain (dark areas on C).

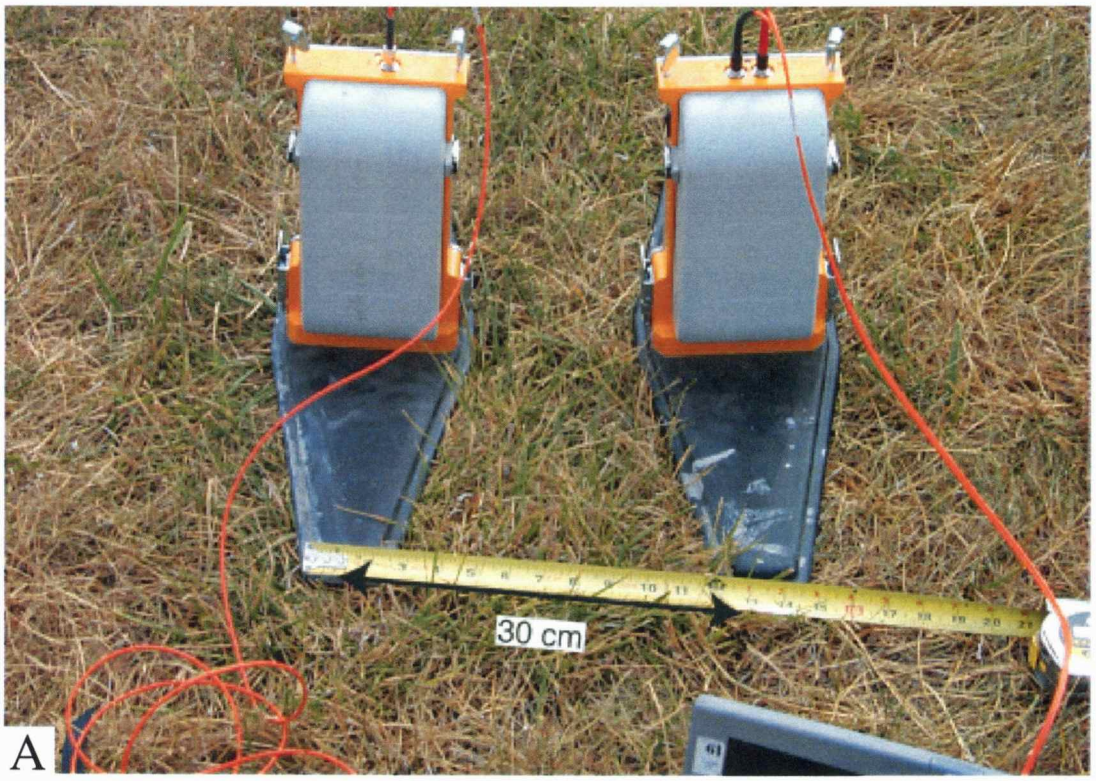

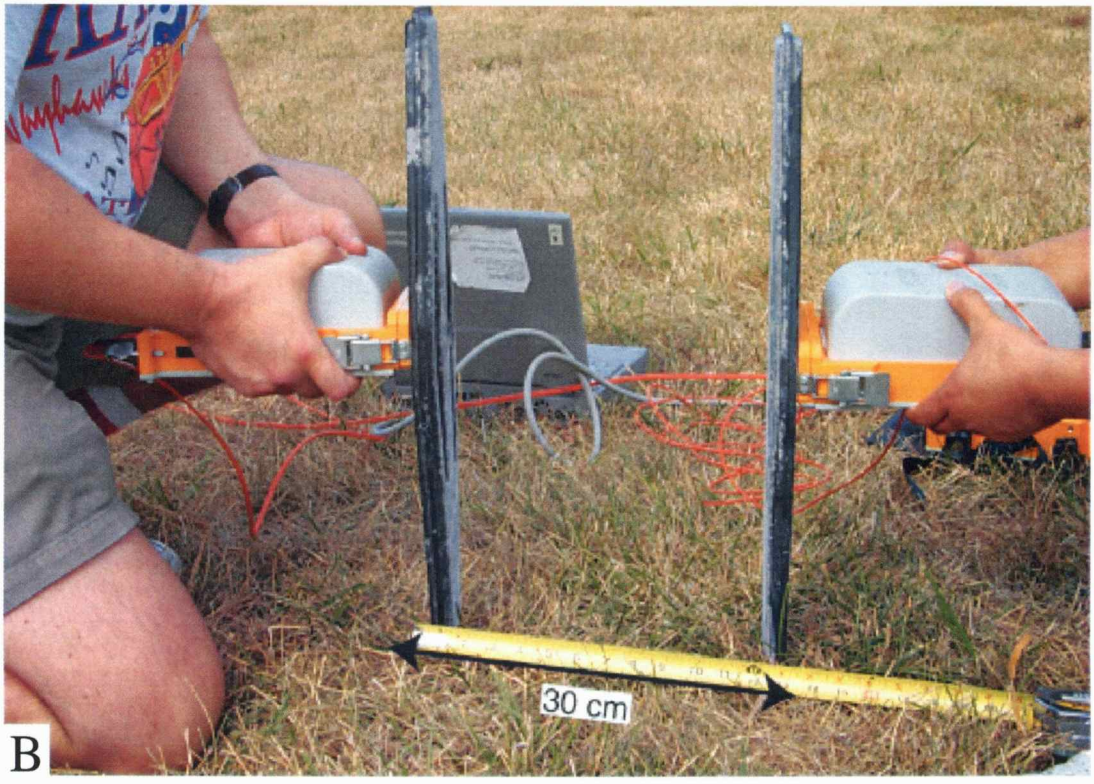

Figure 5: Methodology for capturing source wavelet for 400 Mhz antennas. A) Transmitter antenna and receiver antenna separated by 0.3 m, using conventional facedown on the ground coupling. B) The antennas were then placed face to face in the air at 0.3,m to acquire the actual source wavelet.

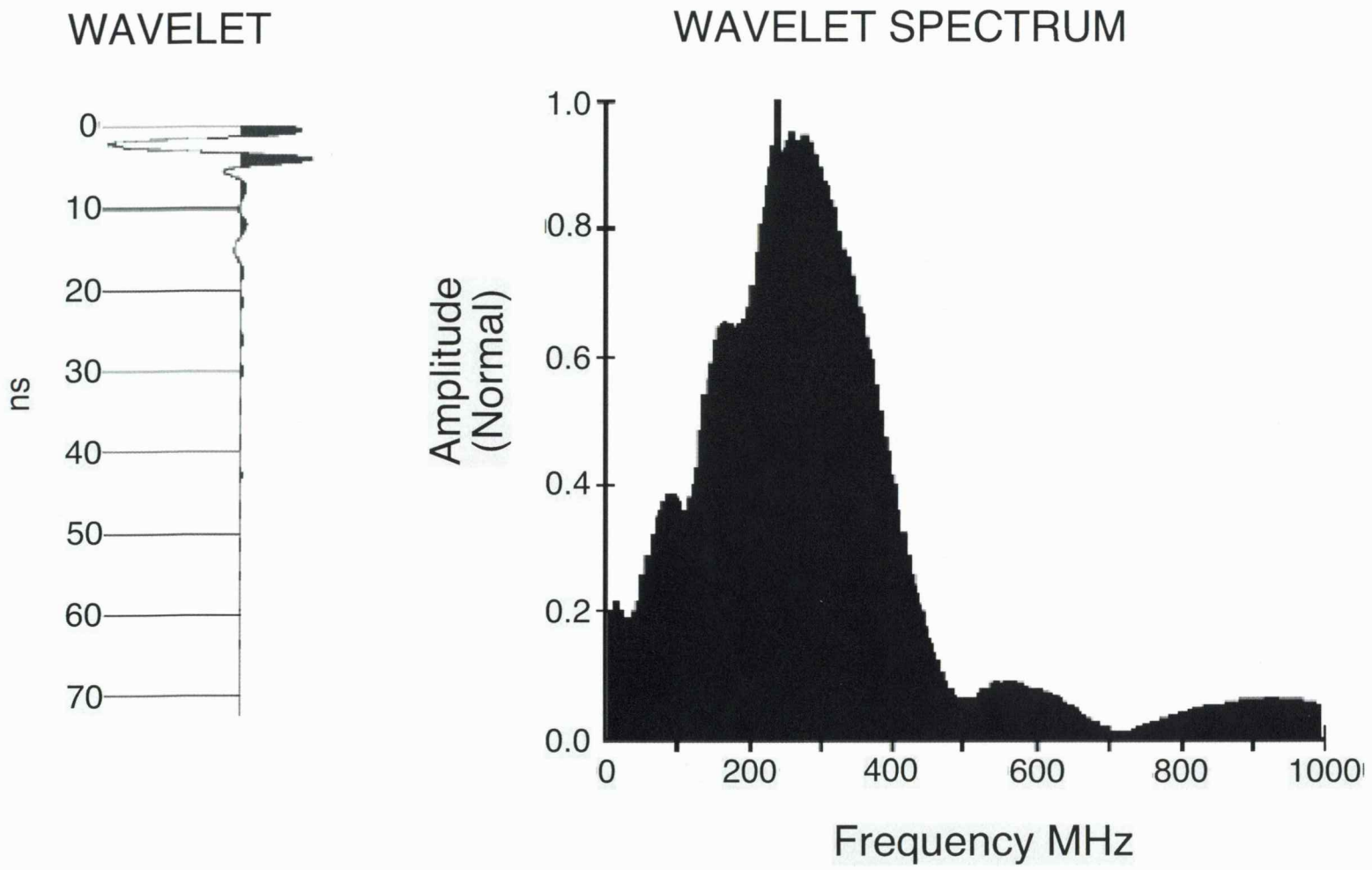

Figure 6: Wavelet characteristics for 400 MHz antennas with 0.3 m separation in signal search and wavelet acquisition.

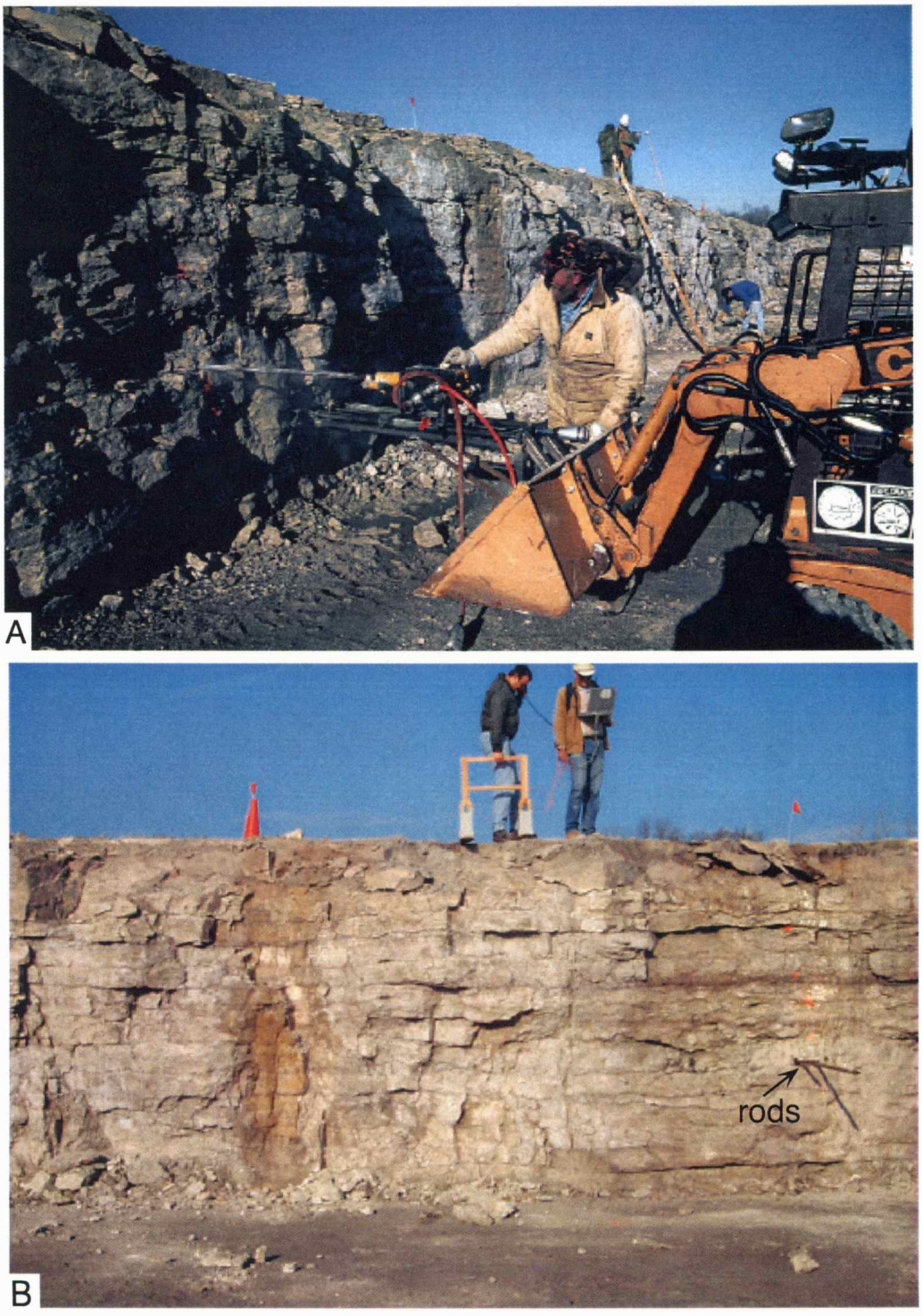

Figure 7: A) A specially designed air drilling unit was used to drill holes that allowed horizontal rods to be inserted into the quarry face. driven snuggly into place.
B) Steel rods, 1.5 m in length and 4.4 cm in diameter, were inserted into holes in quarry faces for groundtruthing of GPR data.

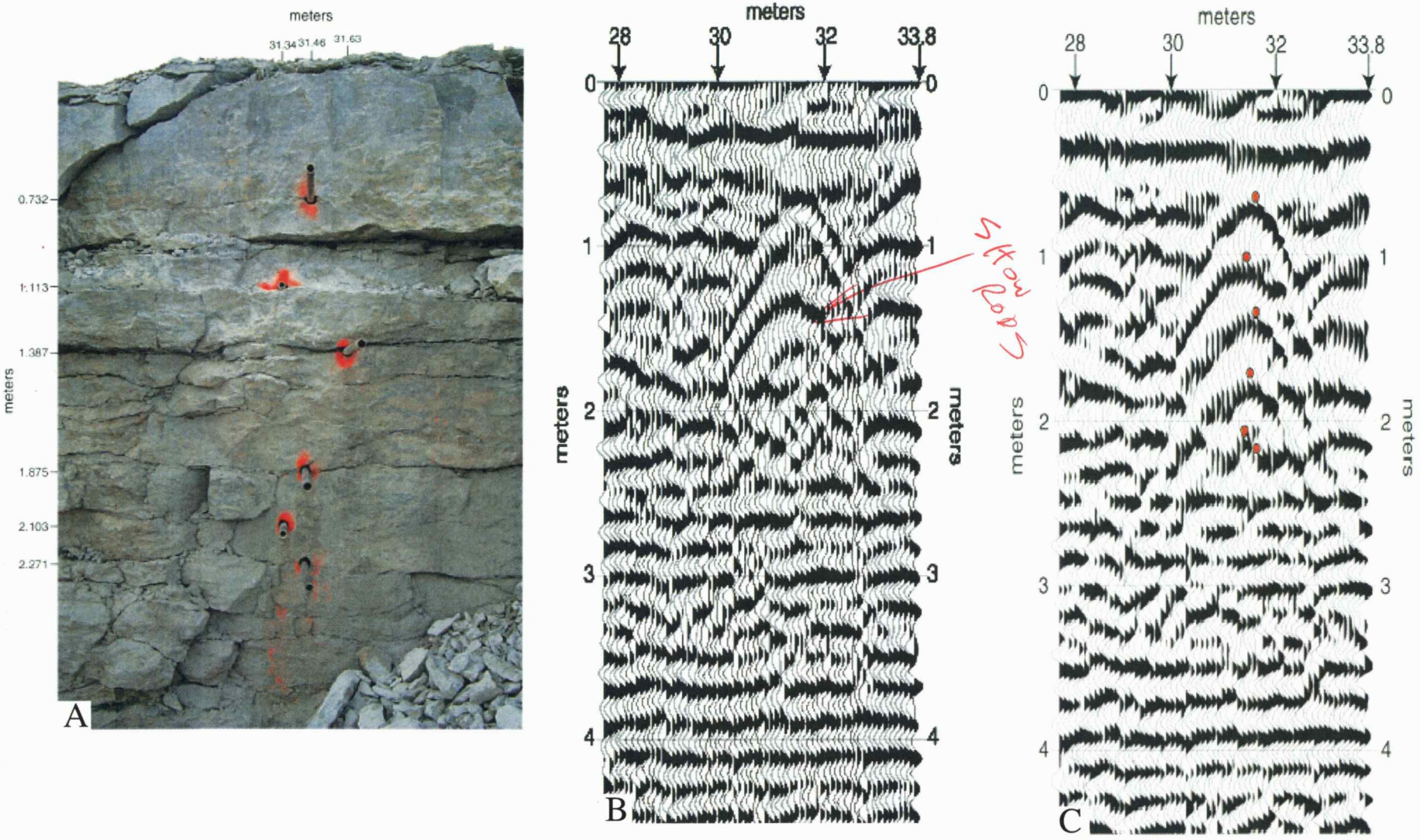

Figure 8: A) Experiments using conductive metal rods to demonstrate effectiveness of deterministic deconvolution. B) Results on conventional GPR data (scaled and bandpass filtered). C) Resutls on GPR data after deterministic deconvolution. The theoretical maximum vertical resolution at the site is ~0.25-0.3 m for the 400 MHz antenna. On the conventionally processed data, resolution of rods is relatively poor and rod locations are skewed compared to true locations as measured on quarry face. In contrast, after applying deterministic deconvolution, resolution is significantly improved (by > 50% in some cases) and locations of rods are spatially accurate.

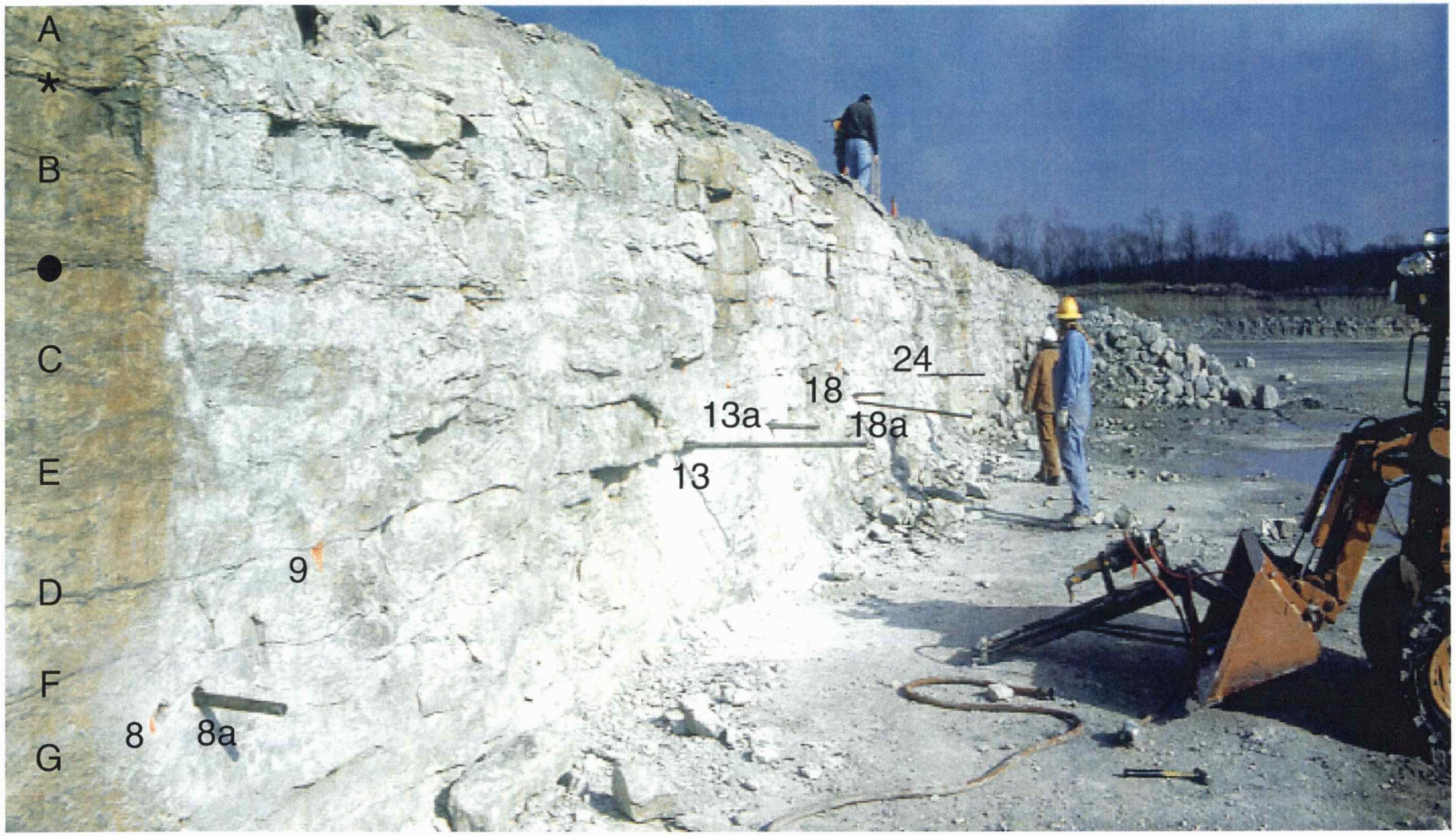

Figure 9: Rods were variously placed and arranged laterally along horizons or vertically stacked- (Fig 8) along exposures to determine nature of GPR response and for use in accurately calibrating GPR data to known locations as measured on the quarry face. Letters indicate beds; numbers indicate rod locations.

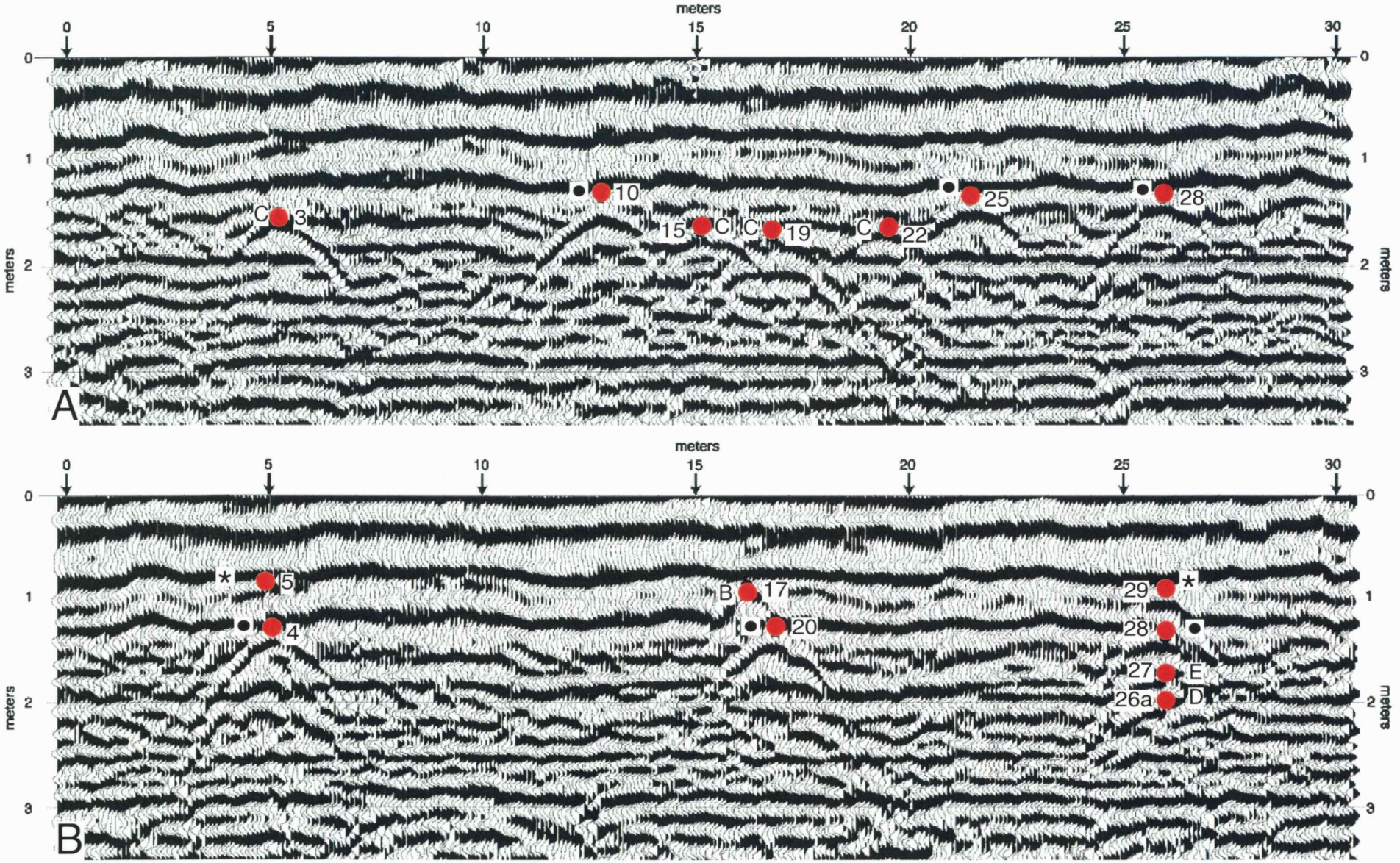

Figure 10: Results of some of the rod experiments carried out on BSG1. Orange dots and numbers are rod locations. Letters and symbols are bed identifications. Note, these GPR data include the deterministic deconvolution processing step. Common-midpoint (CMP) data were acquired and velocities of EM wave propagation were calculated based on moveout curves on the CMP data for time to depth conversion. The accuracy of these calculated depths were compared to actual locations of steel rods for verification.

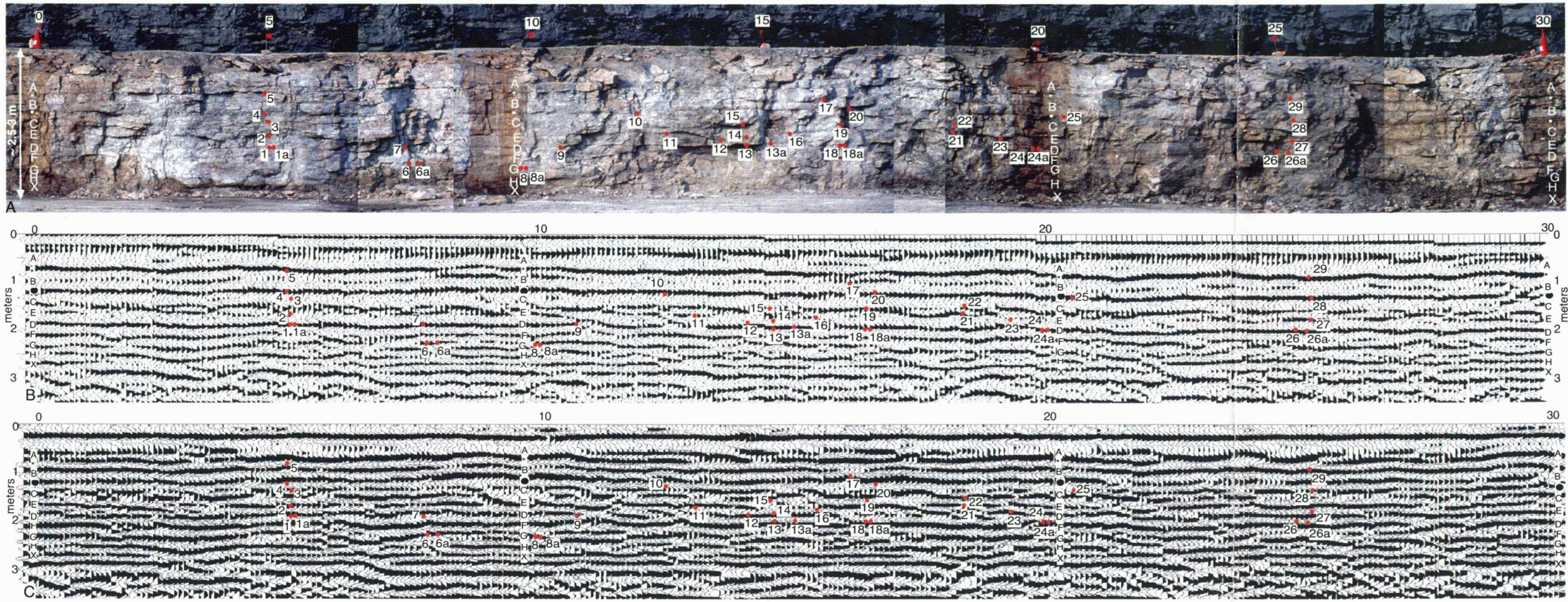

Figure 11: Comparison of GPR data from BSG1 quarry face (A) after deterministic deconvolution processing (B) and the same GPR data after just AGC scaling and bandpass filtering (C), which are the type of data conventionally used for interpretation in sedimentary studies. Note the complexity in C compared to B. GPR reflections on B (after deterministic deconvolution) are easier to directly tie to geologic features on the photo mosaic and are confirmed by steel rod data (orange dots).

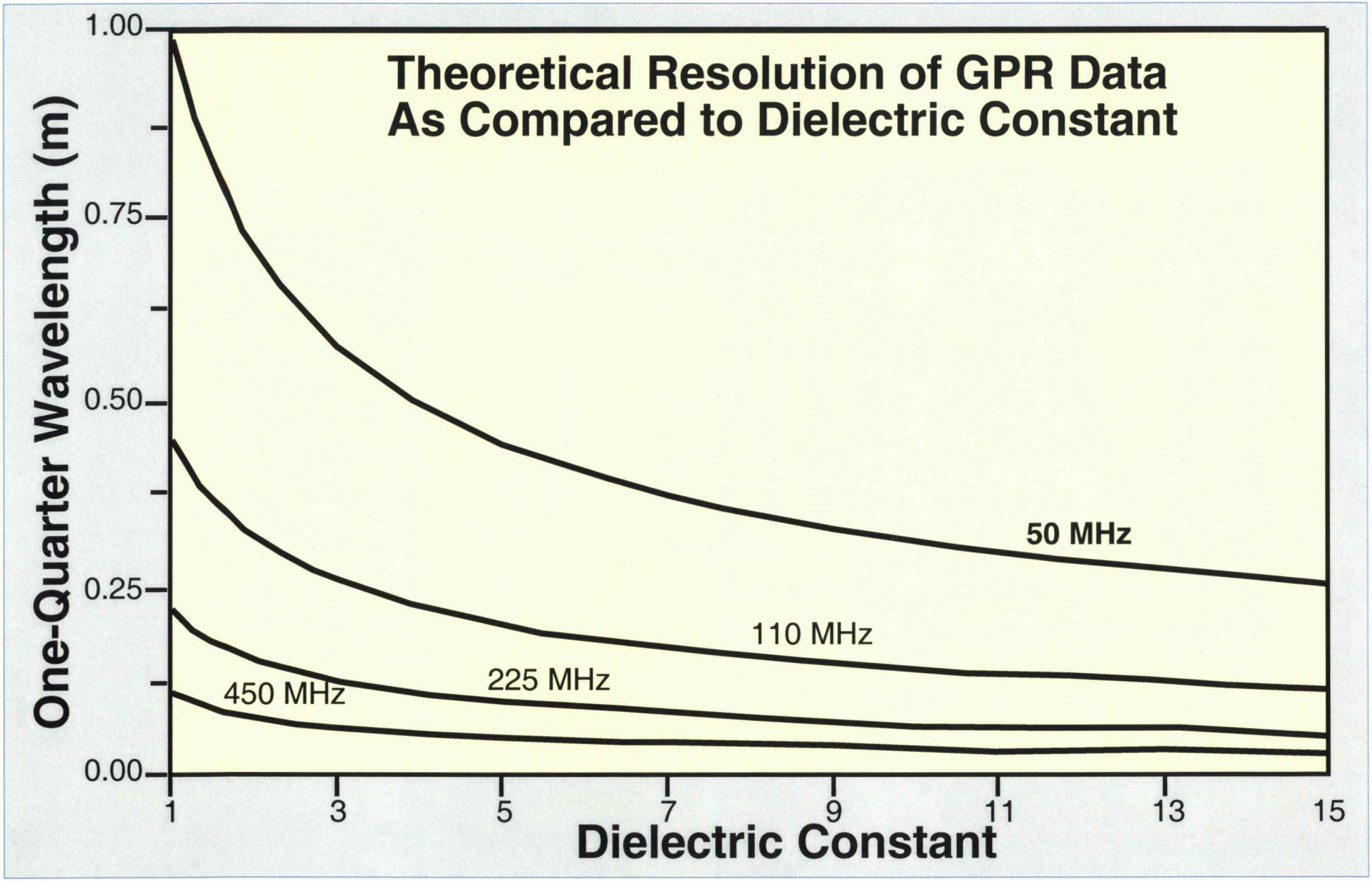

Figure 12: Theoretically, resolution should be at least ~15 cm and potentially greater, depending on dielectric constant, using the 400 MHz antenna.

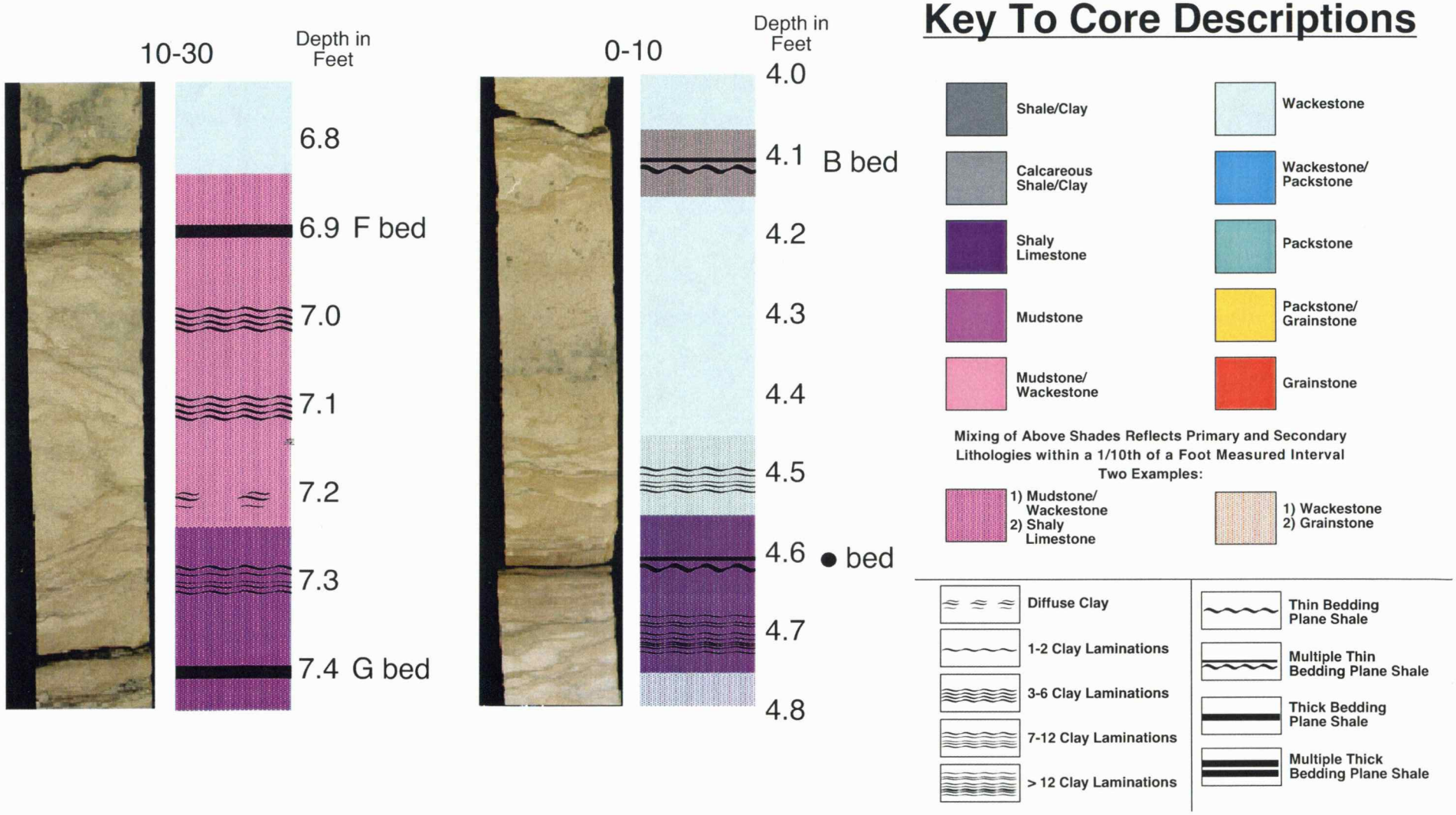

Figure 13: Examples of cores and core descriptions. The core on the left is from the BSG2 face (10 meters back from original BSG1 face and at the 30 m lateral location along the face. The core on the right is from the BSG1 face at the 10 m location laterally along the face. The key also applies to cores displayed on photomosaics and GPR lines of Figures 14, 15, 16, and 17.

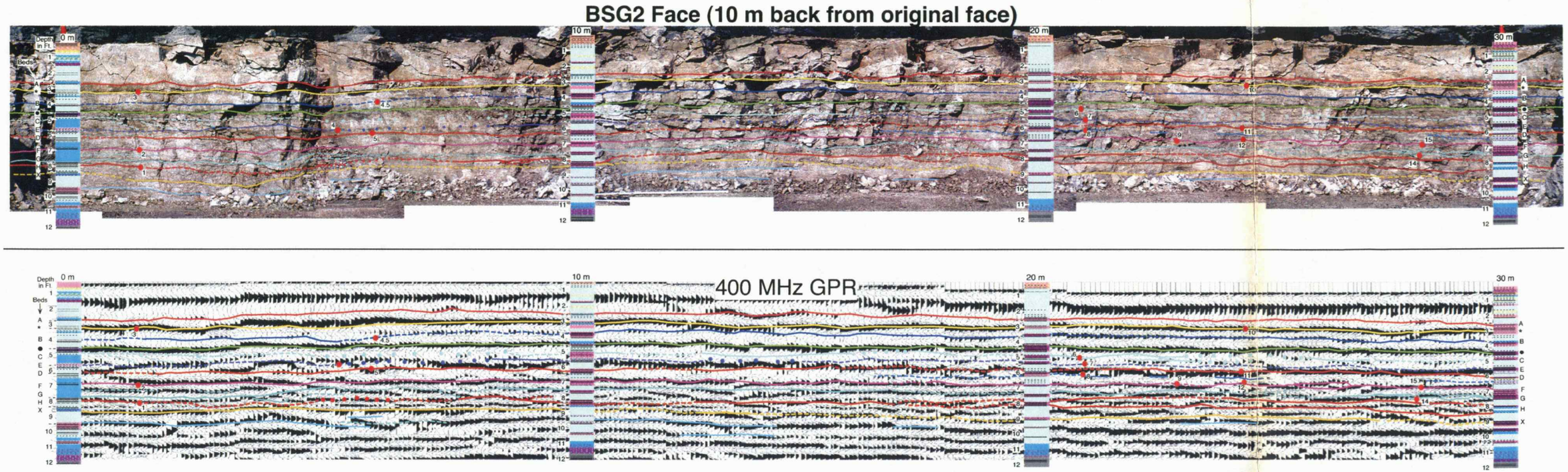

Figure 14: Photomosaic (with cores) shows facies and bedding characteristics as traced on the photo during study of the exposed quarry face. These traces are essentially shown directly overlain on GPR data from the same face; exact locations are confirmed by steel bar experiments. Solid lines represent distinct, traceable bedding planes (shale partings), dashed lines reflect where bedding planes are less distinct (shale partings are thinner or more diffuse), and dotted lines represent inferred bedding planes. Orange dots show locations for horizontal conductive bar experiments. GPR data were taken with 400 MHz antennas 1 meter behind the BSG1 quarry face. See Figure 13 for key to core descriptions.

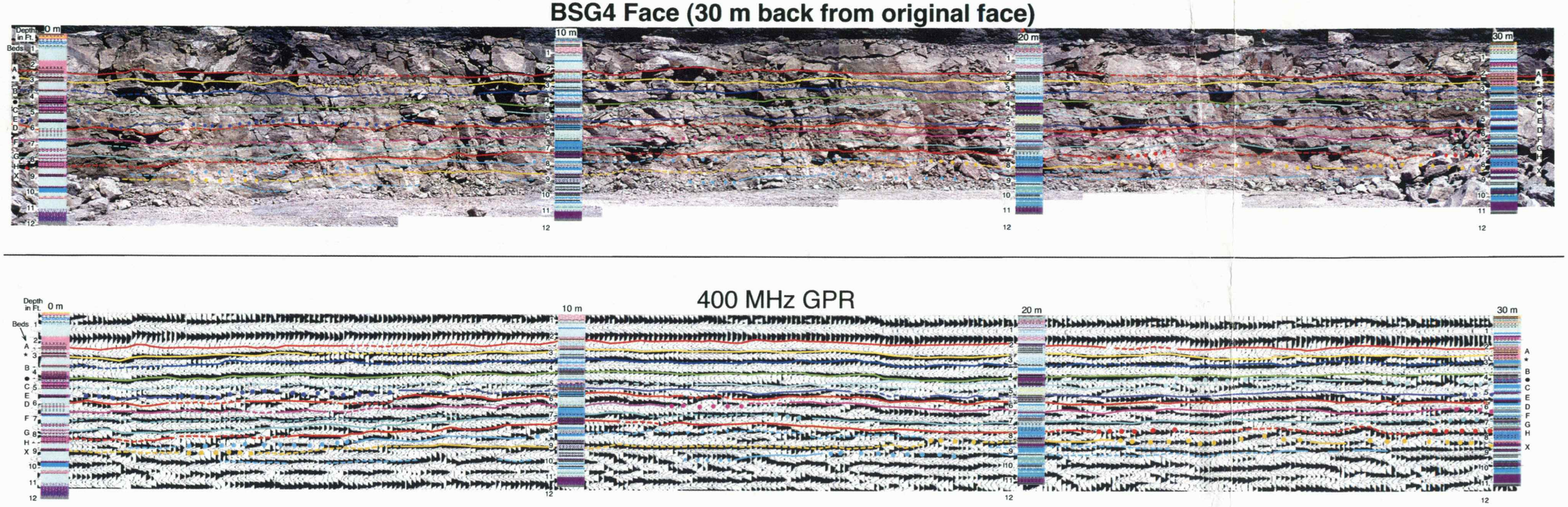

Figure 15: Photomosaic (with cores) shows facies and bedding characteristics as traced on the photo during study of the exposed quarry face. These traces are essentially shown directly overlain on GPR data from the same face; exact locations are confirmed by steel bar experiments. Solid lines represent distinct, traceable bedding planes (shale partings), dashed lines reflect where bedding planes are less distinct (shale partings are thinner or more diffuse), and dotted lines represent inferred bedding planes. Orange dots show locations for horizontal conductive bar experiments. GPR data were taken with 400 MHz antennas 1 meter behind the BSG1 quarry face. See Figure 13 for key to core descriptions.

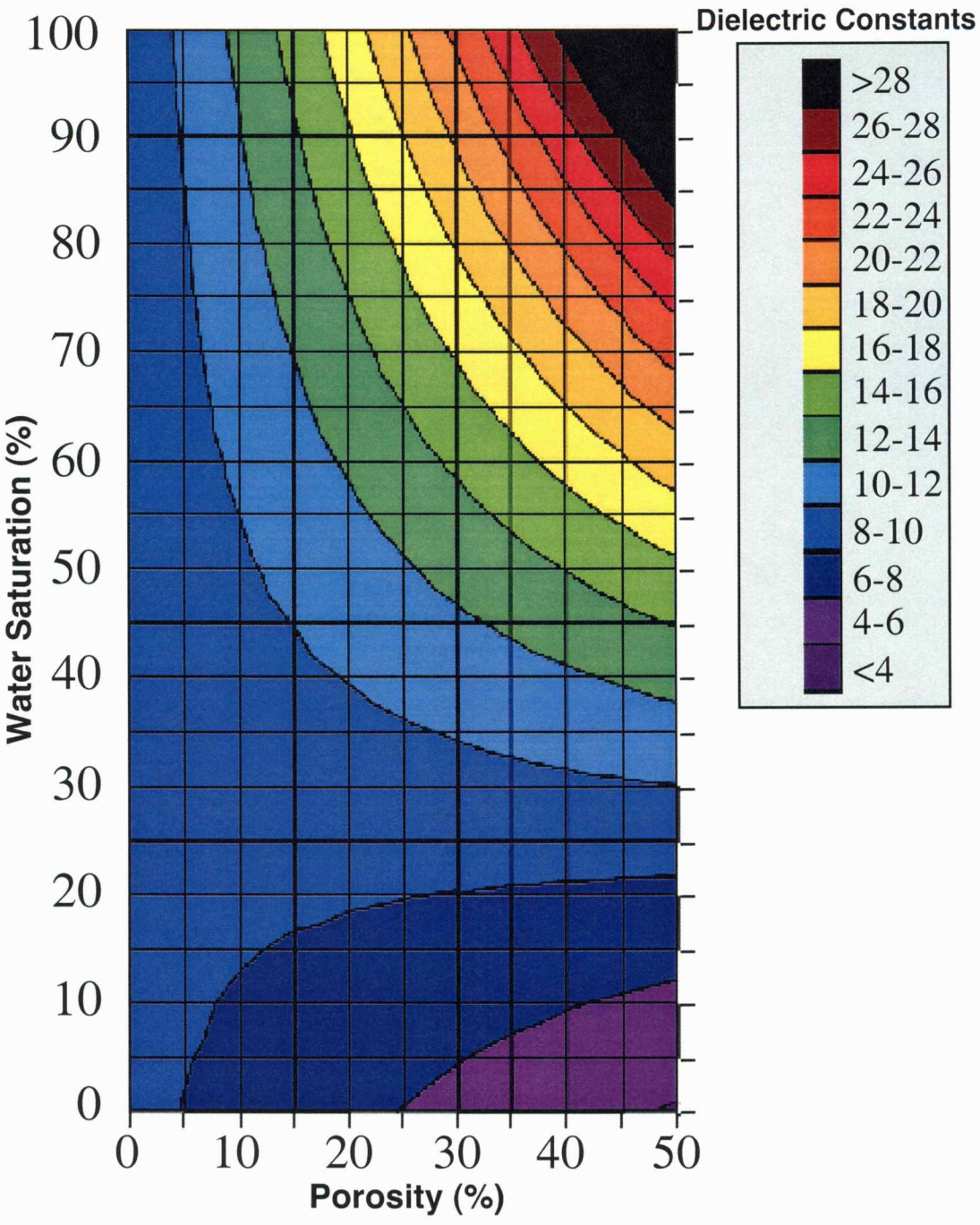

Figure 16: Bulk dielectric constant is controlled to a first order by water saturation and to a second order by porosity and mineralogy, although these variables are interdependent. Bulk dielectric constant values can range from 2 to 38 for typical non-clayey materials depending on mineralogy, porosity, and water saturation.

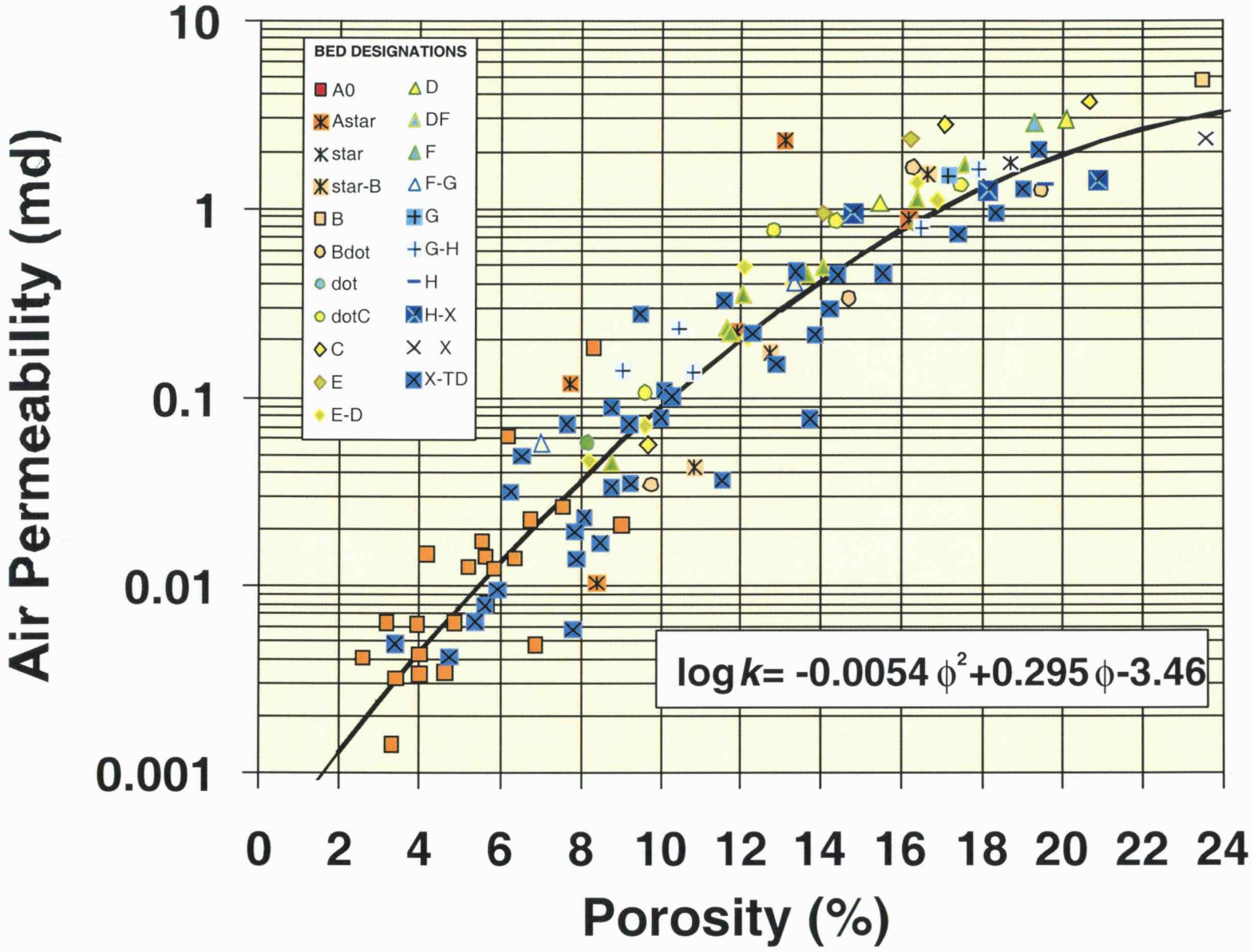

Figure 17: Plot of porosity and air permeability. Permeability is highly correlated with porosity for all beds

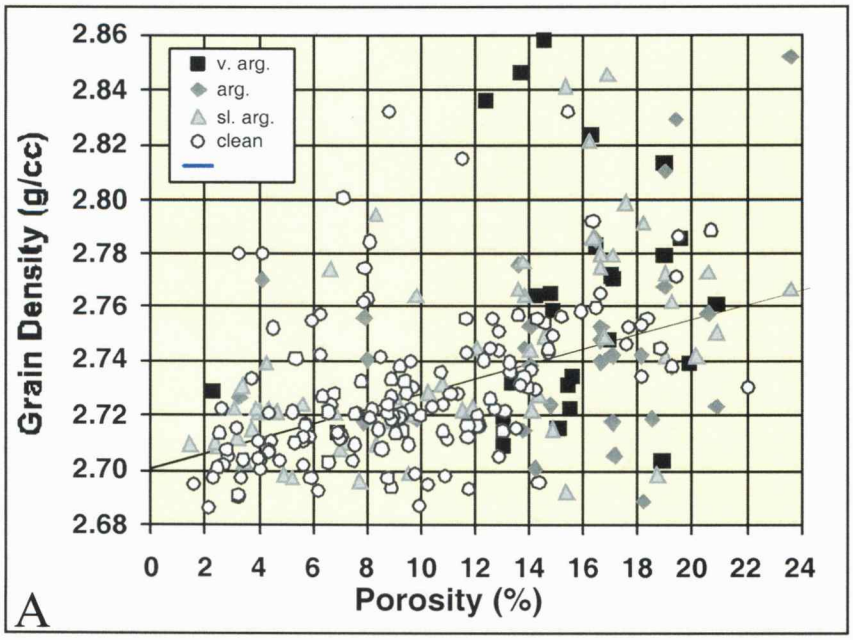

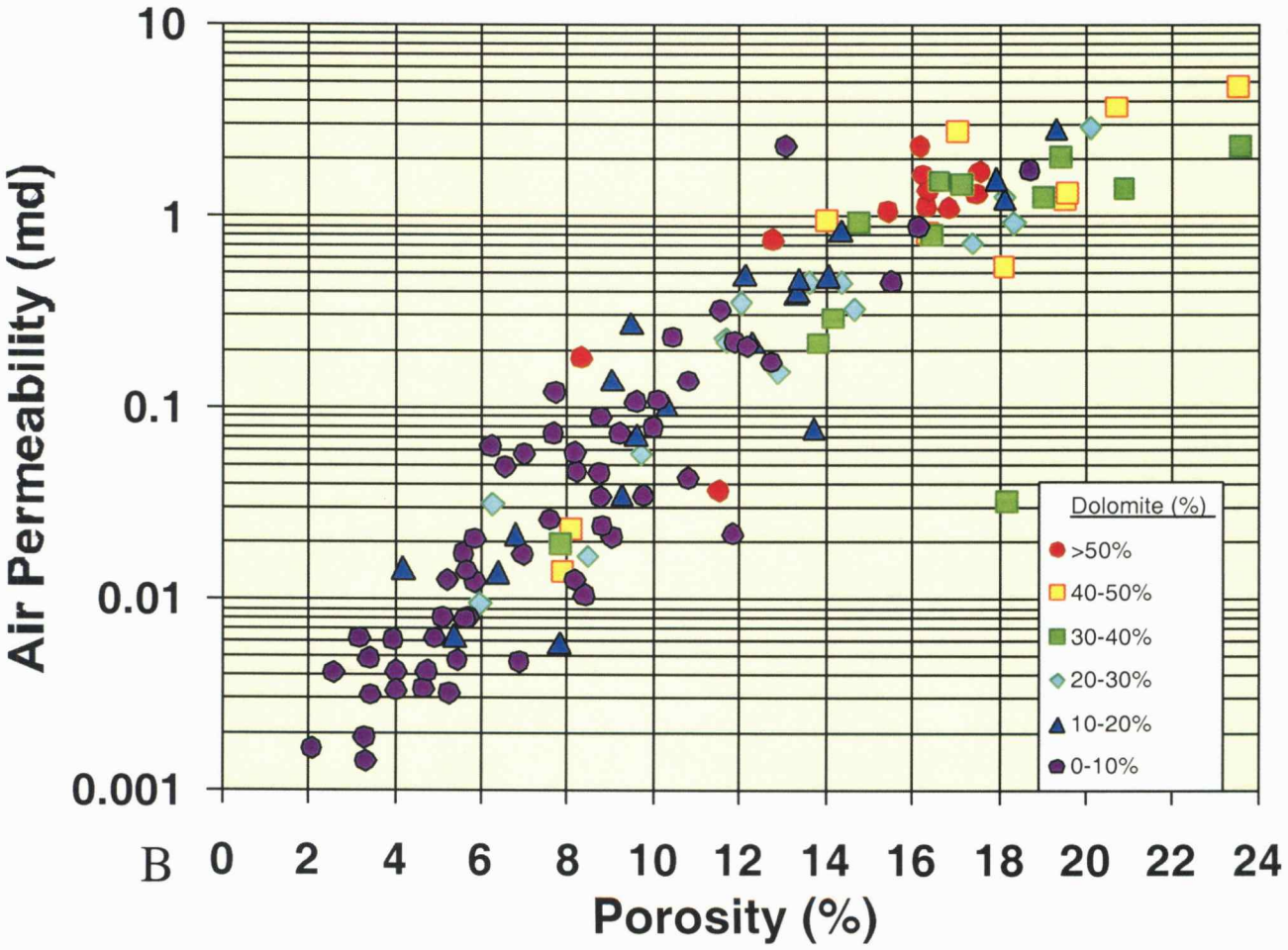

Figure 18: A) Plot of porosity versus grain density. Grain density increase is related to increase in amount of dolomite. B) Plot of porosity versus air permeability. Symbols and colors indicate differing percentages of dolomite.

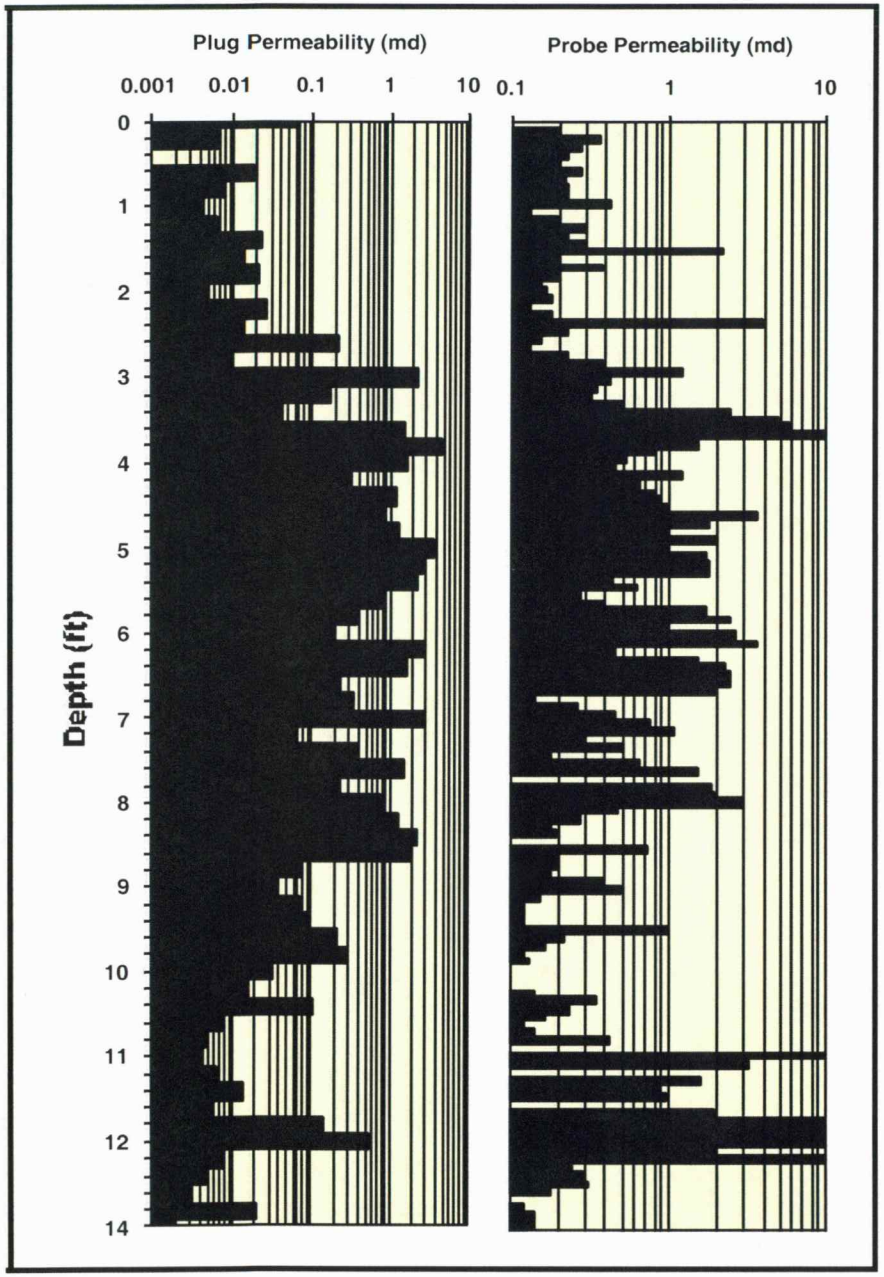

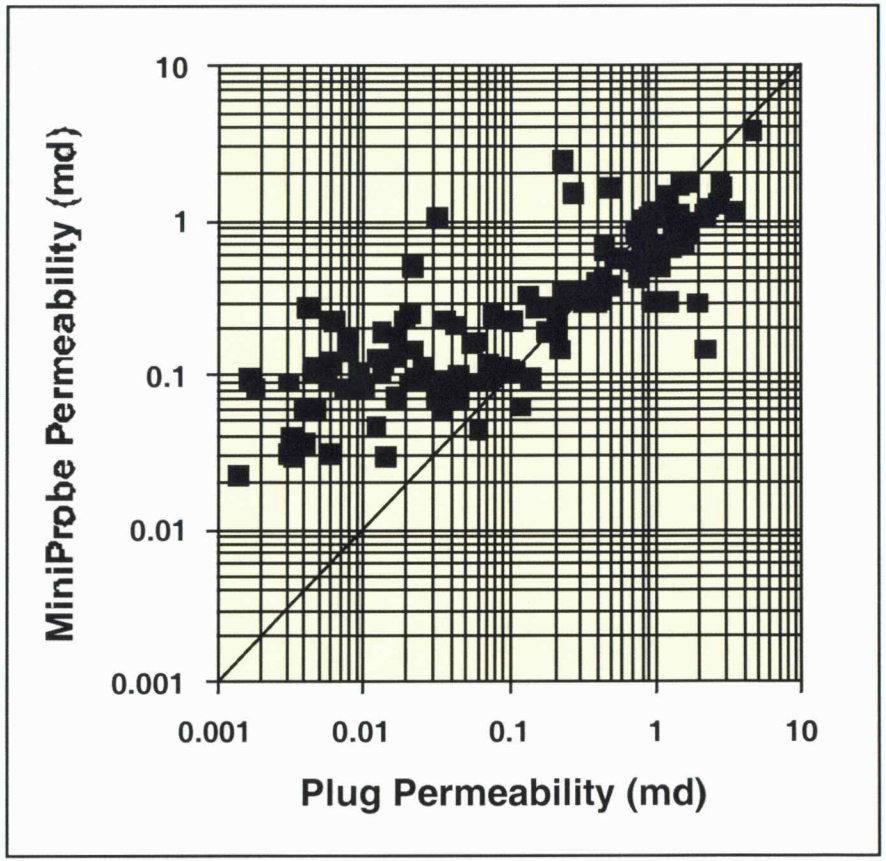

Figure 19: Comparisons of plug permeability with miniprobe permeability. The good correlation between *k* and f potentially allowed the prediction of f from easily measured probe permeability measurements. Those measurements were well correlated with the more accurate plug values for $k > 0.1$ md, but probe values were not accurate at low *k* and are not useful for f prediction in this low range.

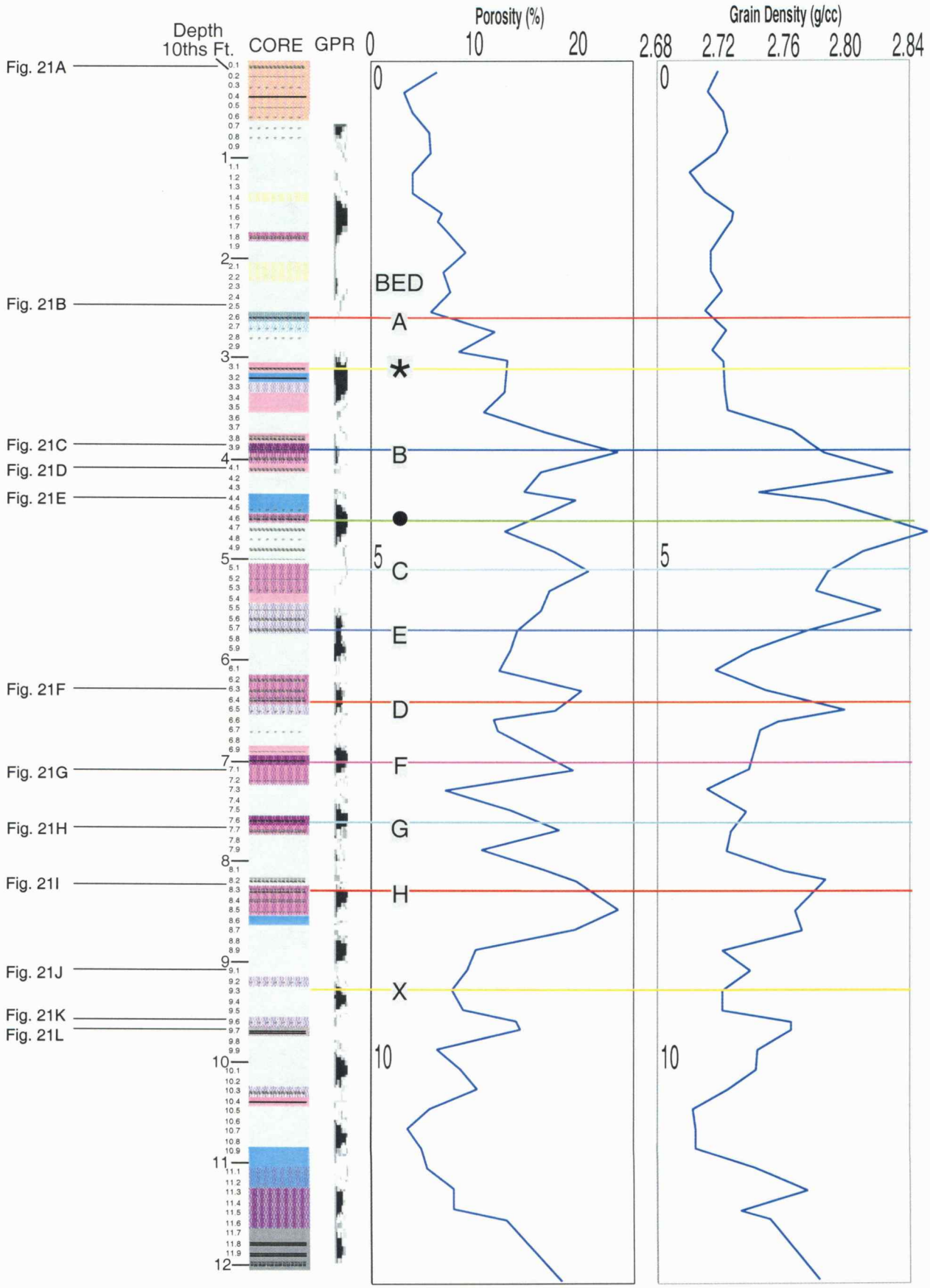

Figure 20: Lithologic features, rock properties, and GPR response for the 10-10 core. Increasing grain density is generally indicative of increase in amount of dolomite. Increased porosity is generally associated with dolomite; much of the dolomite is associated with clay-rich intervals. Higher porosity also is associated with partings along clay-rich beds. Note locations of photomicrographs (Figs. 21A-L) showing lithologic details. See Figure 13 for key to core descriptions.

A

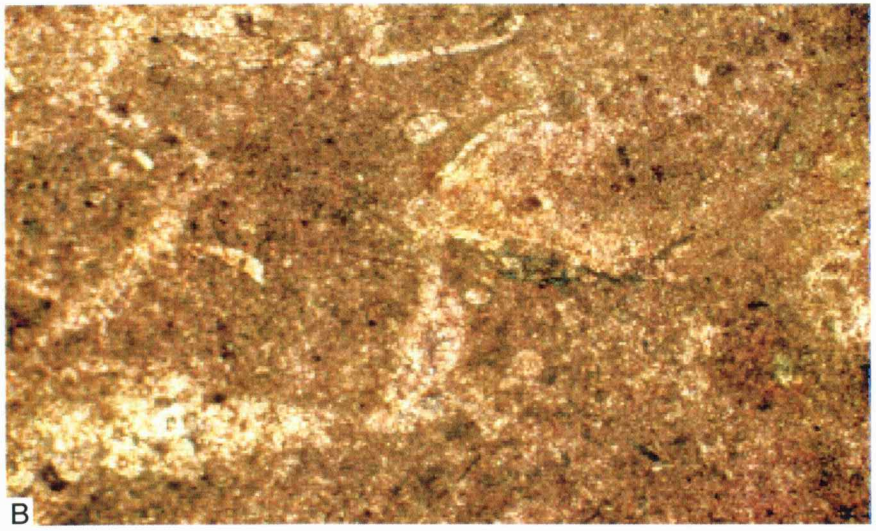

B

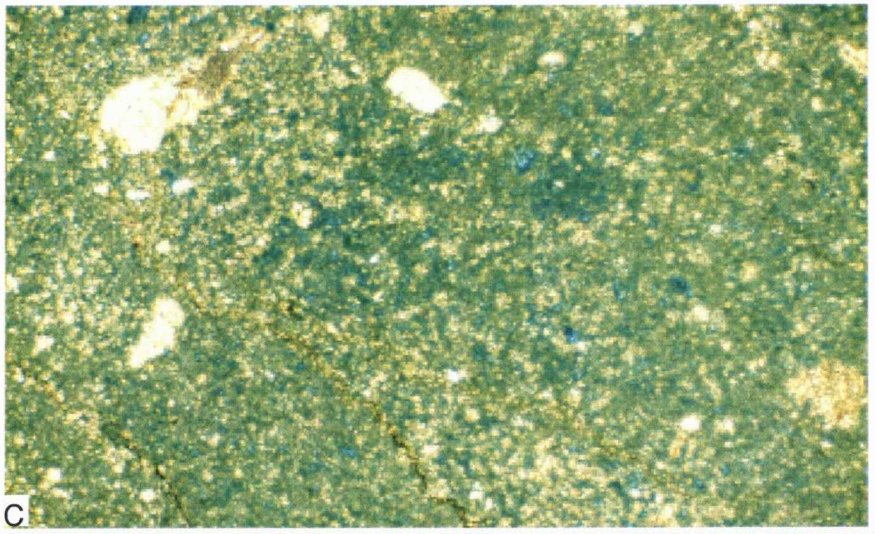

C

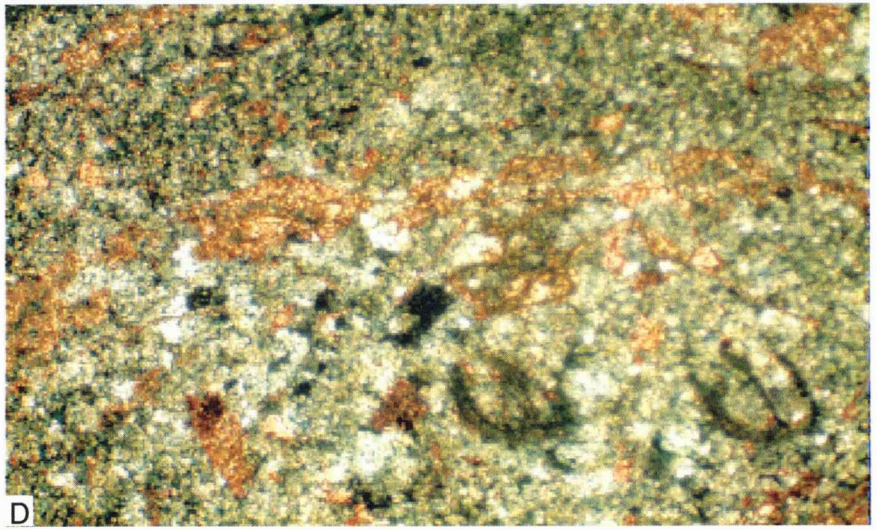

D

Fig. 21 A) 0.1 feet - Skeletal wackestone/packstone with clay-rich stylocumulates and concentrated skeletal fragments. 6.2 % porosity .062 md permeability 5% dolomite. Dual stain; red is calcite. Field of view (long dimension) is 5 mm. B) 2. 5 feet - Phylloid, brachiopod, bryozoan wackestone. 5.7% porosity. Perm = .014 md. 0% dolomite. Dual stain; red is calcite. Field of view is 5 mm. C) 3.9 feet - Shaly skeletal fragment wackestone. 23.5% porosity. Permeability = 4.7 md. Dolomite = 47%. Note the blue-green color is due to blue epoxy filling in microporosity. No stain. Field of view is 5 mm. D) 4.1 feet - Bryozoan, brachiopod, phylloid algal wackestone with some clay.16.3 % porosity. Permeability = 1.65 md. Dolomite = 74%. Dual stain; red is calcite, clear is dolomite. Dolomite in this interval is mixture of matrix dolomite and coarser dolomite cement. Field of view is 5 mm.

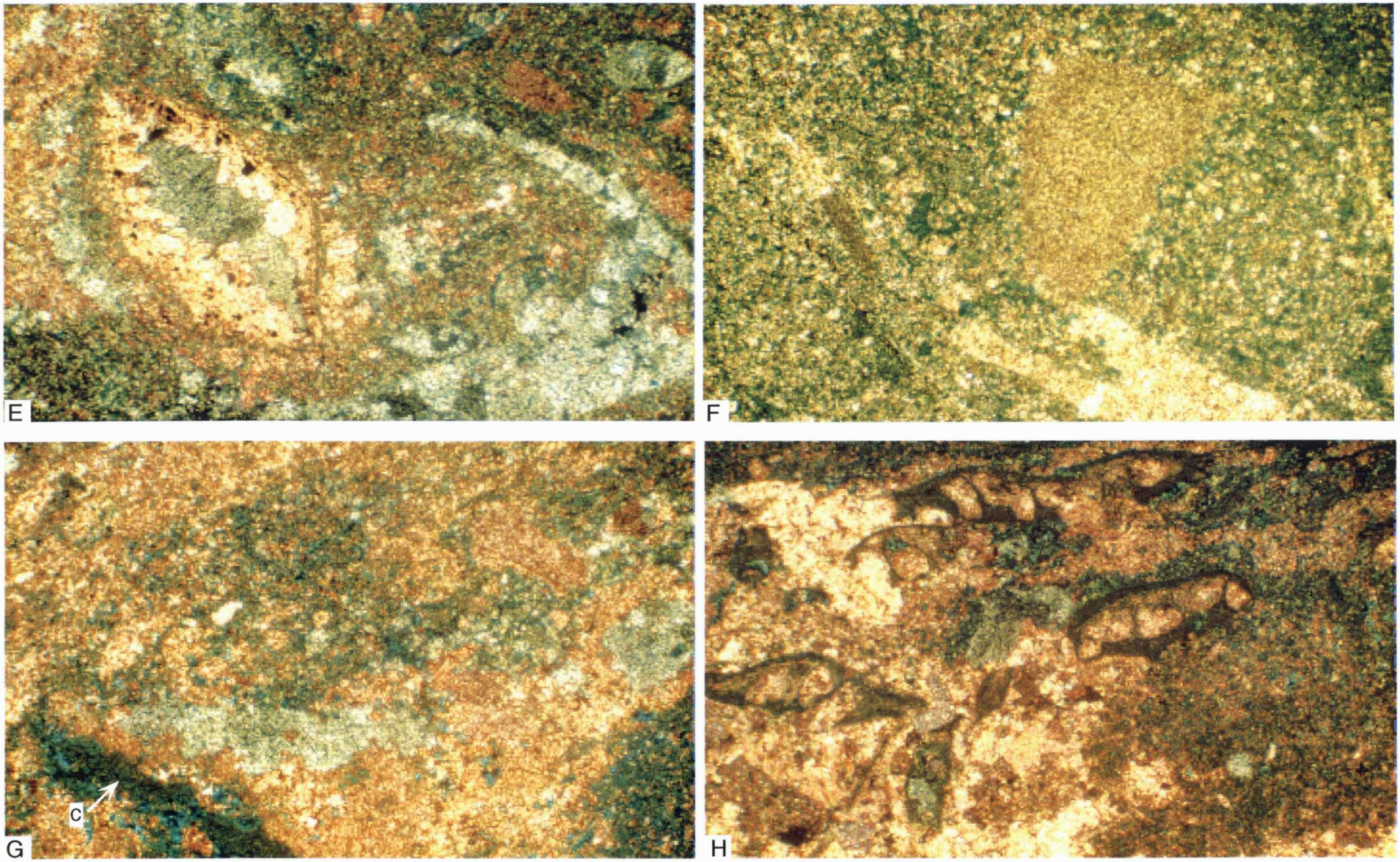

Fig. 21: E) 4.4 feet - Brachiopod, phylloid algal, bryozoan wacketone/packstone. 19.5% porosity. Permeability = 1.24 md. Dolomite = 48%. Dual stain; red is calcite, clear is dolomite. Field of view is 5 mm. F) 6.3 feet - Shaly bryozoan, echinoderm, brachiopod, phylloid algal mudstone/wackestone. 20% porosity. Permeability = 2.92 md. Dolomite = 24%. No stain. Field of view is 5 mm. G) 7.1 feet - Skeletal fragment wackestone with some clay (c). 19.3% porosity. Permeability = 2.85 md. Dolomite = 17%. Dual stain; red is calcite clear is dolomite. Field of view is 5 mm. H) 7.7 feet - Shaly, bryozoan, phylloid algal, brachiopod wackestone. 18% porosity. Permeability = 1.60 md. Dolomite = 10%. Red stained areas are calcite. Field of view is 5 mm.

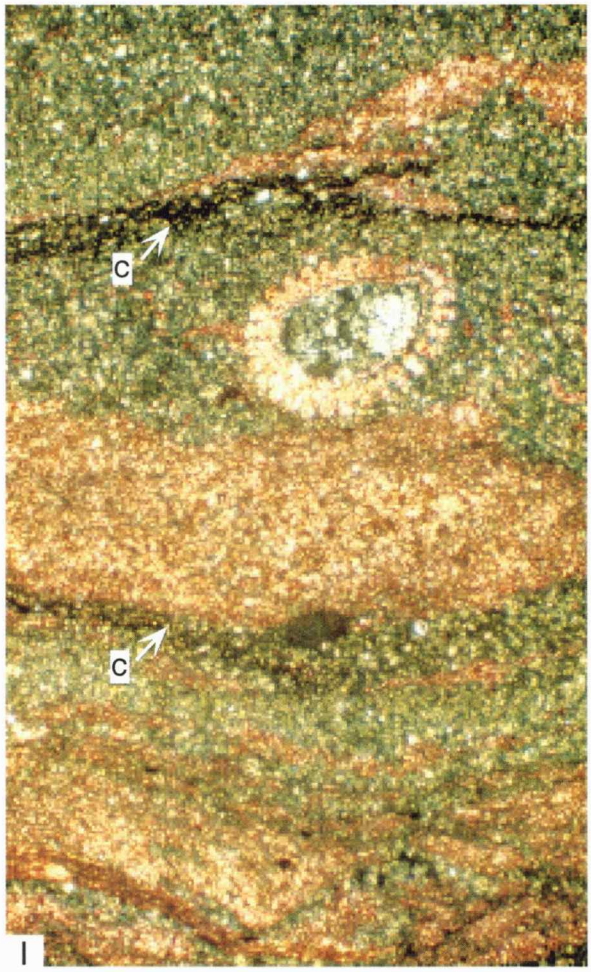

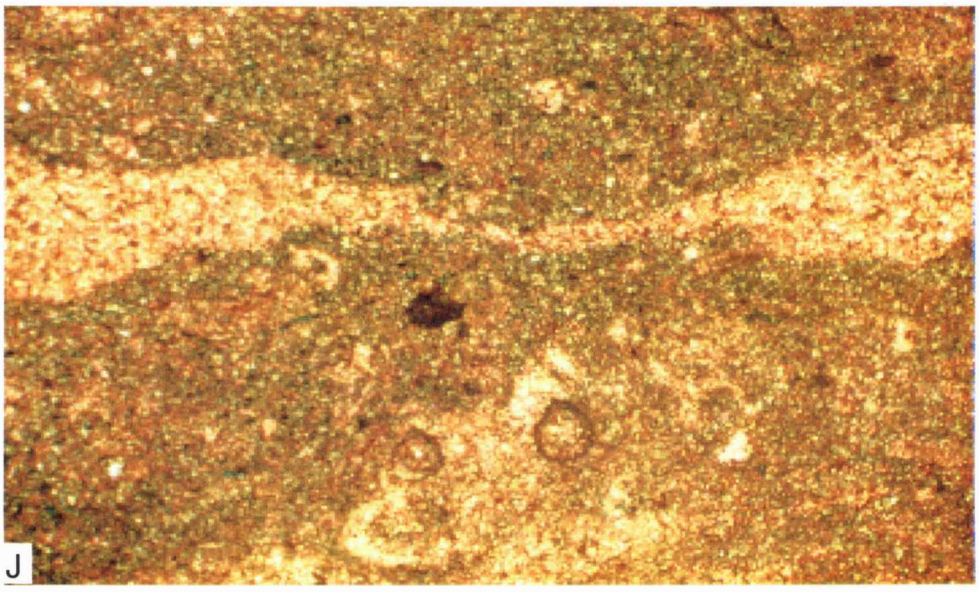

Fig. 21: I) 8.25 feet - Shaley skeletal wackestone with thin clay seams (c). 19.6% porosity. Permeability = 1.3 md. 47% dolomite. Dual stain; Red is calcite, clear and darker areas are dolomite and clay. Field of view is 5 mm. 9.1 feet - Phylloid algal, bryozoan, skeletal fragment wackestone. J) 9% porosity.Permeability = .035 md. Dolomite = 18%. Dual stain; red is calcite,clear and darker areas are dolomite and clay. Field of view is 5 mm.

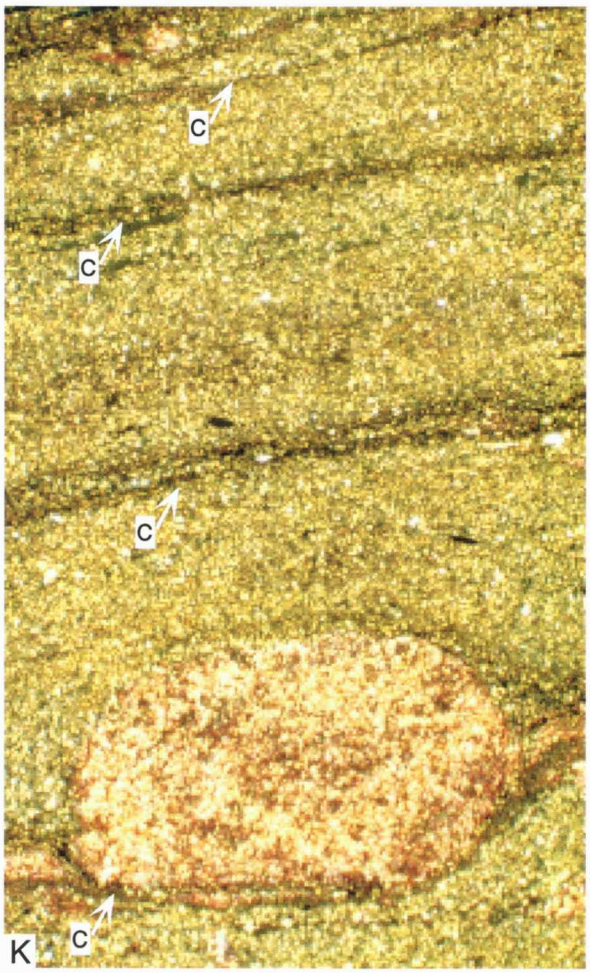

Fig. 21: K) 9.6 feet - Shaly skeletal fragment wackestone with clay-rich stylocumulates (c). 13.8% porosity. Permeability = .215 md. Dolomite = 34%. Dual stain; red is calcite, clear and darker areas are dolomite and clay. Field of view is 5 mm. L) 9.7 feet - Shale-rich skeletal fragment wackestone. 14% porosity. Permeability = .03 md. Dolomite = 34%. Dual stain; red is calcite, clear and darker areas are dolomite and clay. Field of view is 5 mm.

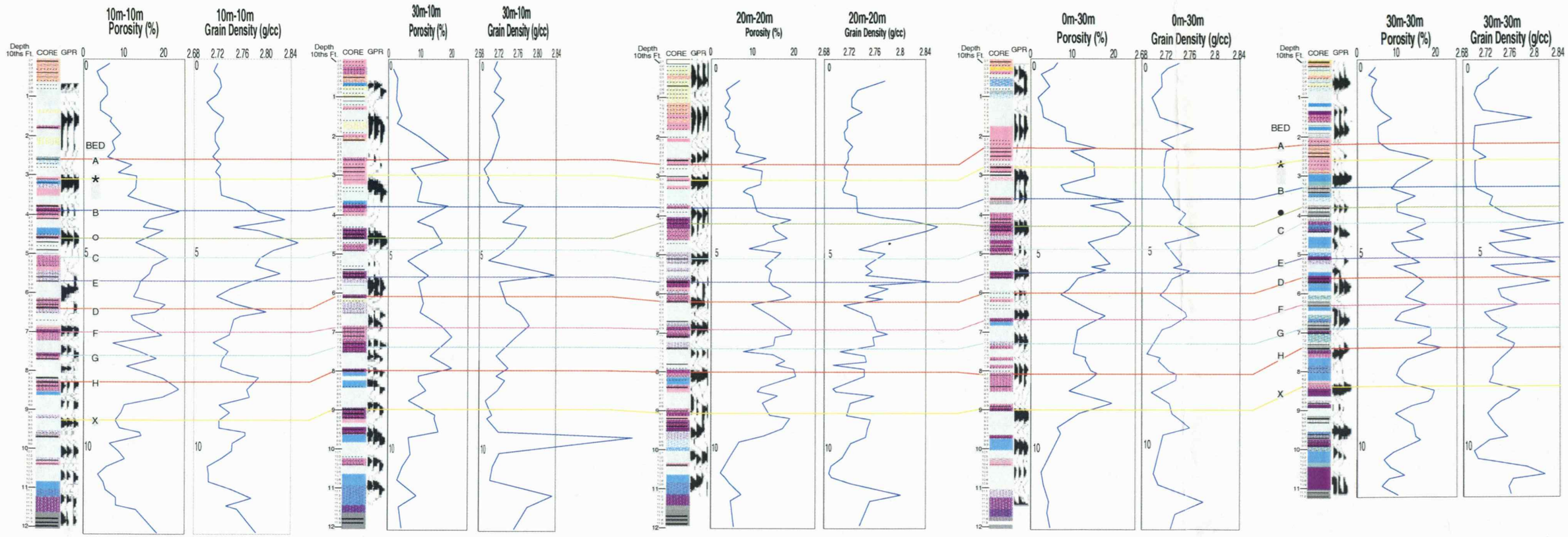

Figure 22: Comparison and correlation of lithology, GPR response, porosity, grain density between five cores from three different quarry faces.
See Figure 13 for key to core descriptions.

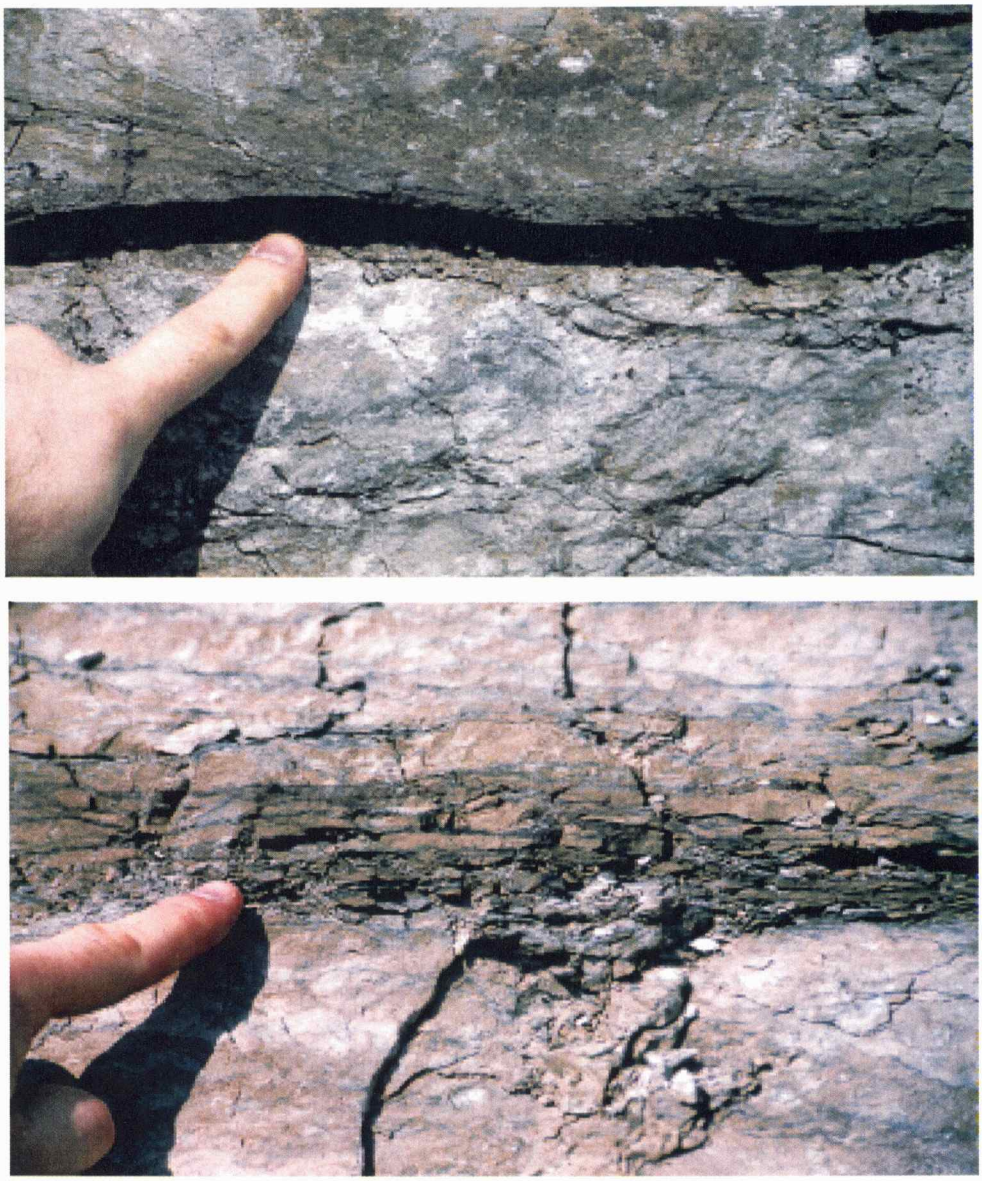

Figure 23: Water seeped out along horizontal partings in shales and saturations in the limestone overlying shales or between fine shale beds approached 100%. High water saturations, and associated high E_r, and high E_r for shales containing clays with high surface area and cation exchange capacity, both significantly control the reflectance coefficient.

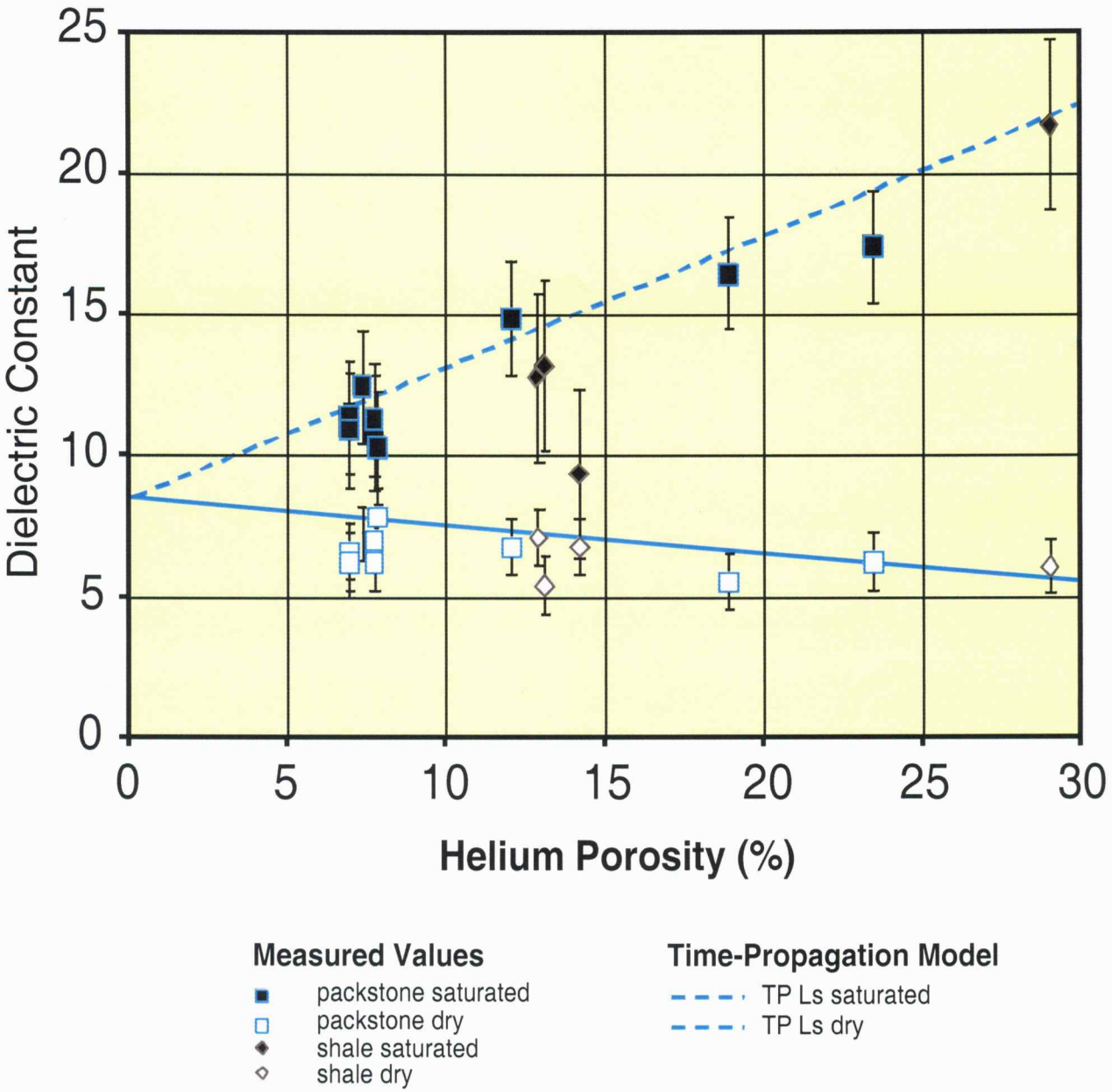

Figure 24: Time propagation (TP) models of the strata at the quarry site confirm that this modeling approach is sufficiently accurate for larger scale forward modeling.

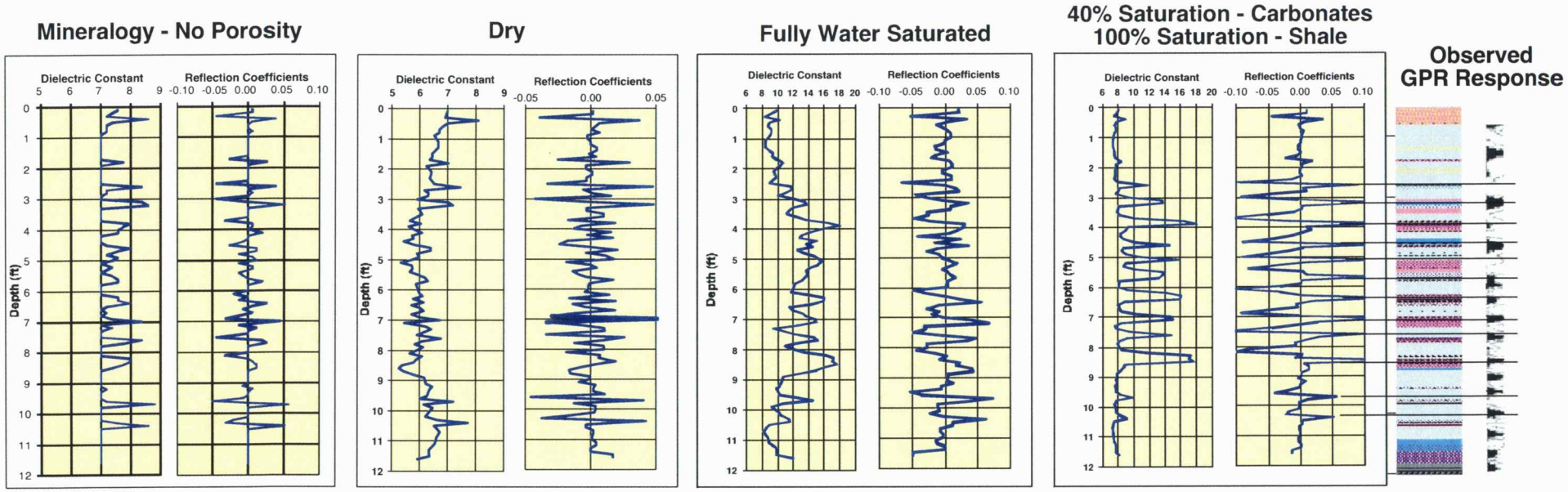

Figure 25: Time Propagation modeling shows that mineralogy alone at the site cannot account for the observed GPR response. Modeling also shows that a dry or fully water-saturated outcrop does not exhibit the observed GPR response. Note that full water saturation reverses reflectance polarity. Modeled response for a profile with ~40% saturation in the limestone and 100% in the shales exhibits strong RC values at the shale beds and closely matches observed GPR response.